Atmospheric correction and inherent optical property estimation in the southwest New Caledonia lagoon using AVNIR-2 high-resolution data

Hiroshi Murakami, Cecile Dupouy

1 # Atmospheric correction and inherent optical property

2 ## estimation in the southwest New Caledonia lagoon using

3 ## AVNIR-2 high-resolution data

4

5 **Hiroshi Murakami[1,*], Cécile Dupouy[2]**

6 *[1] Japan Aerospace Exploration Agency, Earth Observation Research Center, 2-1-1, Sengen,*

7 *Tsukuba, Ibaraki, Japan 305-8505*

8 *[2] Aix-Marseille University, University of South Toulon Var, CNRS/INSU, IRD, MIO, UM 110*

9 *Centre IRD of Noumea, BP A5, 98848, Noumea, New Caledonia*

10 **Corresponding author: murakami.hiroshi.eo@jaxa.jp*

Abstract

12 Retrievals of inherent optical properties (IOPs) and Chlorophyll-a concentration (*Chla*) was

13 investigated for AVNIR-2 images with 30-m spatial resolution and four bands in the southwest

14 tropical lagoon of New Caledonia. We corrected the atmospheric and sea-surface reflectance

15 iteratively through the retrieval of IOPs. After an additional correction of sea floor reflectance,

16 the estimated IOPs and *Chla* agreed well with the in situ measurements even in the lagoon

17 areas. This study provides a method to allowing a local optimal estimation of IOPs and *Chla*

18 with a high resolution sensor by preparation of the candidate spectra for the target areas.

19

1. INTRODUCTION

1.1 Ocean color retrievals in the coastal areas

Ocean color retrieval is a challenge in the coastal areas but is a powerful tool for coastal surveys. Sea surface reflection, including sunglint and whitecap, cause significant errors in the ocean color estimation [1,2,3]. Sea surface reflection can be estimated from a statistic scheme such as that presented by Cox and Munk [4] using low-resolution wind speed data from a microwave radiometer, a scatterometer, or objective analysis data (e.g., [5,6]). However, the correction based on the wind speed data is problematic in coastal areas because of fine variations in the distribution of surface reflection due to variable winds, fetch length, and air-sea stability caused by the fine structure of the coastal geography. Several studies have investigated high spatial resolution sunglint correction using hyperspectral bands or small scale glint variations (e.g. [7,8]). Murakami and Frouin [9] demonstrated the possibility of sunglint (ρ_g) correction by using 500-m resolution near infrared (NIR) and shortwave infrared (SWIR) bands of Moderate Resolution Imaging Spectroradiometer (MODIS). Higher (10-30 m) spatial resolution sensors are expected to capture higher resolution spatial structures of ocean color phenomena, especially in the coastal areas. However, they have a limited number of spectral bands generally (*e.g.*, without SWIR bands), which prevents the precise estimation of aerosol properties and the distinction between aerosol and sea-surface reflection.

In addition to these sensor limitations, coastal areas present difficulties for ocean color retrievals, *i.e.*, high NIR reflectance by suspended matter, complex Inherent Optical Properties (IOPs) due to various material inputs from the land, and bottom reflectance in the shallow areas. This explains why the blue/green ratio of remote sensing reflectance (R_{rs}), which is

42 traditionally used in the empirical estimation of chlorophyll-a concentration (*Chla*), does not

43 allow to calculate *Chla* in most cases of the coastal area (see Table 1 for symbol definitions

44 and units).

1.2 The New Caledonia lagoon

46 The New Caledonia lagoon is a large, almost continuous lagoon (22177 km^2) lying in the

47 southwestern tropical Pacific from 20°S to 22°S and 166°E to 167°E (Fig. 1). Its heterogeneous

48 bathymetry (25 m as a mean depth) is due to a complex geomorphology with the presence of

49 sedimentary plains and a high proportion of shallow waters and numerous small sand islands

50 [10,11,12]. It is largely connected to the open ocean along its southern side, but only by narrow

51 passes in its southwestern side. It is an example of a coral reef lagoon system, which are very

52 sensitive to anthropogenic (nutrients, mining) perturbations [10,11] as well as to interannual

53 changes linked to the balance between dry El Niño and wet La Niña episodes [13,14], which

54 are amplified in lagoons [12]. The central lagoon is characterized by oligotrophic to

55 mesotrophic waters (yearly average chlorophyll-a concentration of 0.25 ± 0.01 mg m^{-3}) [15,16]

56 and exhibits a strong seasonal cycle with higher values in austral winter (July) or austral

57 summer (February) during nitrogen-fixing *Trichodesmium* blooms [17,18,19,20]. Upwelling at

58 the barrier reefs [21] as well as internal waves in the southern part of the lagoon are two major

59 mechanisms of exchange with the sea, which can modify the phytoplanktonic assemblage [22].

60 Rain can also induce large chlorophyll enrichments in the lagoon [23]. With relatively low

61 river inputs and a low turbidity range (0.20-16 g m^{-3}), its trophic state is linked to spatial

62 variations in flushing times [12,16,24]. Similarly to "optically complex" Case 2 European

63 waters [25] or coastal bays [26], reflectance in the New Caledonia lagoon can be highly

64 variable [27] as in other tropical environments [28], the Australian Great Barrier Reef [29],

65 tropical estuaries [30] with a high influence of mineral particles from river discharge in bays

66 [31] or colored dissolved organic matter (CDOM) [32]. Additionally, bottom reflectance,

67 which represents a strong component in clear tropical shallow waters, may influence R_{rs}

68 [33,34,35,36].

69 In order to improve the challenge of remote sensing in coastal environments [37], surface

70 water IOPs (absorption and backscattering) were measured during several observation

71 campaigns (e.g., coastal stations of Diapalis in 2003, Bissecote, Echolag, Valhybio, and the

72 Valhybio Monthly Survey cruises from 2006 to 2010) in the lagoon and at different seasons

73 [27,38,39]. The bathymetry of the Southern New Caledonia lagoon was compiled [12].

74 ## 1.3 ALOS AVNIR-2

75 Advanced Land Observation Satellite (ALOS) has been operated by JAXA from 24 Jan.

76 2006 to 12 May 2011 and carried the Advanced Visible and Near Infrared Radiometer type 2

77 (AVNIR-2). AVNIR-2 has four spectral bands (centered at 463 nm, 560 nm, 652 nm, and 821

78 nm) with a 10-m Instantaneous Field of View (IFOV), a 70-km Field of View (FOV) and a

79 mechanical pointing function (by moving mirror) along the cross-track direction (±44 deg) for

80 effective global land observation. To achieve the ALOS mission objectives (cartography,

81 regional observation, disaster monitoring, resources survey, and technology development) and

82 to expand to quantitative applications, such as determination of vegetation density, coastal

83 water color and their time dependencies, it is important to evaluate, improve and maintain the

84 radiometric calibration accuracy of AVNIR-2 (the pre-defined target is absolute error less than

85 10% [40]). The cross-calibration with MODIS indicated that the difference in top of

86 atmosphere (TOA) radiance is less than 3% in the visible bands, and the temporal stability of

87 the radiance is less than 2% per 1000 days [41].

88 1.4 Scope of this study

89   Atmospheric and sea surface correction and IOP estimation were conducted using the four

90 bands of 30-m images averaged from AVNIR-2 10-m images (see section 2.1). The linear

91 matrix inversion (LMI) of IOPs [42,43,44] and atmospheric + surface reflection correction was

92 simplified to allow the four-band and high spatial resolution AVNIR-2 retrievals. Influence of

93 the bottom reflectance was reduced by using bathymetry data with a unique spectrum of

94 bottom reflectance. We compared the IOP estimates by different candidate IOP spectra

95 (observed particles + CDOM absorption (a_{pg}) and particle backscattering (b_{bp}) spectra) in the

96 LMI scheme. *Chla* was estimated by two ways, from a statistical relationship with a_{pg}, or from

97 blue/green ratio of R_{rs}. For the series of AVNIR2 images available over the New Caledonia

98 lagoon, we validated the derived IOPs (a_{pg} and b_{bp}) and *Chla* using in situ measurements

99 around the AVNIR-2 observation dates.

100 **2. DATA AND METHODS**

101 2.1 AVNIR-2 images and radiance correction

102   AVNIR-2 data have 10-m spatial resolution but only 8-bit digital resolution with relatively

103 low gain designed for the land-surface observations. We averaged AVNIR-2 TOA radiance

104 images to a 30-m (0.0003 degrees equal latitude-longitude) grid to reduce the sensor noise

105 before the atmospheric correction because the ocean-color signal is much lower than

106 atmospheric one in the visible wavelengths.

107   The AVNIR-2 in-orbit radiometric performance was evaluated through a comparison with

108   Aqua MODIS by the cross-calibration scheme [41]. This scheme uses the TOA reflectance

109   functions of the satellite zenith angle estimated by Aqua MODIS observations within ±16 days

110   from the AVNIR-2 observation over temporally and spatially stable ground areas. The cross

111   calibration with the Aqua MODIS over the Antarctic snow fields allow us to correct AVNIR-2

112   bands 1-4 by the correction coefficients shown in Table 2. We calculated the TOA reflectance

113   of standard gas absorption conditions (column ozone = 343.8DU, water vapor = 14.19 mm, and

114   pressure = 1013.25 hPa) from the AVNIR-2 radiance observation as shown in Appendix.

115   Seventeen clear AVNIR-2 scenes were captured around the target area in the ALOS

116   mission period. The dates were 10 Sep. and 27 Sep. in 2006, 12 Feb., 3 Mar., 15 May, and 31

117   Jul. in 2007, 31 Oct. and 17 Nov. in 2008, 3 Sep. and 20 Nov. in 2009, 5 Jan., 3 Feb., 21 Mar.,

118   8 Aug., and 22 Dec. in 2010, and 24 Mar. and 10 Apr. in 2011. Some scenes (27 Sep. 2006, 12

119   Feb. 2007, 31 Oct. and 17 Nov. 2008, 20 Nov. 2009, and 5 Jan. 2010) were covered by the

120   sunglint. Match-ups with in situ measurements were obtained (total 15 points) on 3 Sep. 2009

121   (time difference from the AVNIR-2 observation $\Delta D=5$ days), 17-18 Nov. 2009 ($\Delta D=2$ days),

122   and 11 Jan. 2010 ($\Delta D=6$ days).

123   2.2 Simplification of the atmospheric and surface corrections

124   At each solar and sensor geometry condition, the TOA reflectance ρ_t, for which gaseous

125   absorption is normalized by standard atmosphere condition, can be described as follows.

126    $\rho_t(\lambda_b) = \rho_r(\lambda_b) + \rho_a(\lambda_b, \tau_a, M) + t(\lambda_b, \tau_a, M) \times \rho_g(\lambda_b) + T(\lambda_b, \tau_a, M) \times \rho_{wc}(\lambda_b) + T(\lambda_b, \tau_a, M)$

127            $\times \rho_w(\lambda_b)$ (1)

128   where ρ_r is the atmospheric molecule reflectance, ρ_a is the aerosol reflectance, including

129   aerosol-molecule interaction, ρ_w is the water-leaving reflectance, ρ_g is the sunglint reflectance,

130   ρ_{wc} is the whitecap reflectance, t is the atmospheric direct transmittance (sun-surface + surface-

131   satellite), and T is the direct + diffuse transmittance (sun-surface + surface-satellite), λ_b is the

132   center wavelength of sensor spectral band, τ_a is the aerosol optical thickness, and M is the

133   aerosol model. ρ_g can be estimated by a statistical equation [4] using wind speed and the

134   refractive index of water at each wavelength. However, there is no simultaneous 30-m

135   resolution wind speed data, and the statistical relation is not always consistent with the real

136   complicated sea surface.

137   The Rayleigh scattering of ρ_r and T (at $\tau_a=0$) can be estimated by atmospheric radiative

138   transfer simulation. In order to achieve this, we used Pstar2b [45], which takes into account

139   atmospheric polarization, provided by the National Institute for Environmental Studies (NIES)

140   GOSAT project and the OpenCLASTR project [46,47,48]. We prepared look-up tables of

141   $\rho_r(\lambda_b)$ (including sea-surface reflection with wind speed = 0) and T at each geometric condition.

142   The Rayleigh-scattering subtracted reflectance (ρ_{agw}) can be described by the following Eq.

143   (2).

144   $\rho_{agw}(\lambda_b) \equiv (\rho_t(\lambda_b) - \rho_r(\lambda_b)) / T(\lambda_b,\ \tau_a=0)$

145         $= [\ \rho_a(\lambda_b,\ \tau_a,\ M) / T(\lambda_b,\ \tau_a=0) + t(\lambda_b,\ \tau_a,\ M) / T(\lambda_b,\ \tau_a=0) \times \rho_g(\lambda_b) + T(\lambda_b,$

146         $\tau_a=0) \times \rho_{wc}(\lambda_b)\ ] + T(\lambda_b,\ \tau_a,\ M) / T(\lambda_b,\ \tau_a=0) \times \rho_w(\lambda_b)$ (2)

147   The $T(\lambda_{b=1,2,3\ and\ 4},\ \tau_a=0)$ are about 0.83, 0.91, 0.95, and 0.98 respectively at $\theta_{sun}=\theta_{sat}=0$. $T(\lambda_b,\ \tau_a,$

148   $M) / T(\lambda_b, \tau_a=0)$ can be approximated as 1.0 because it is >0.9 when $\tau_a<0.5$. We simplified

149   aerosol and surface reflection ($\rho_{ag} \equiv \rho_a + \rho_g$) as the following form (Eq. (3)) because ρ_{ag} is to

150   be spectrally smooth and can be approximated by a power function α of the wavelength ratio in

151   most cases [49].

152         $\rho_{ag}(\lambda_b) \cong \rho_{ag}(821 \text{ nm}) \times (\lambda_b \times c_{wl} / 821 \text{ nm})^{\alpha}$ (3)

153   The spectral shape of ρ_{ag} was improved by a correction factor, c_{wl} (= 0.99 at band 3 (652 nm)

154   and 1.0 at other bands), which was derived from the atmospheric radiative transfer simulation

155   (the root mean square error of ρ_{ag} is 0.004 at 463 nm for the tropospheric, oceanic, and their

156   mixed aerosols in the case of aerosol optical thickness = 0.3 and air-mass $pl < 4$). The α ranged

157   from -0.5 to $+0.3$ for the oceanic aerosols and from -1.8 to -1.2 for the tropospheric aerosols.

158   The variables about the aerosol and surface reflection, α and ρ_{ag} (821 nm), could be

159   estimated using the AVNIR-2 data through an iteration with the IOP retrieval described in the

160   next section. The approximation of Eq. (3) enabled quick processing including the iteration

161   scheme.

162   2.3   IOP and water-leaving reflectance estimation

163   Most of the IOP algorithms [50] are based on the equation of remote sensing reflectance

164   below the surface (r_{rs}), the total absorption coefficient (a) and the backscattering coefficient

165   (b_b) proposed by Gordon et al. [51].

166         $r_{rs}(\lambda) = g_1 \times u(\lambda) + g_2 \times u(\lambda)^2$ (4)

167         $a(\lambda) = a_w(\lambda) + a_{ph}(\lambda) + a_d(\lambda) + a_g(\lambda)$ (5)

168         $b_b(\lambda) = b_{bw}(\lambda) + b_{bp}(\lambda)$ (6)

169   with

170         $u(\lambda) = b_b(\lambda) / (b_b(\lambda) + a(\lambda))$ (7)

171 where g_1=0.0949 and g_2=0.0794 [51]. a_w, a_{ph}, a_d, and a_g are the absorption spectra of water,

172 phytoplankton, detritus, and CDOM respectively. b_{bw} and b_{bp} are backscattering coefficients of

173 water and particles. Remote sensing reflectance above the surface, R_{rs} is estimated from r_{rs}

174 using the relation from [51,52] as:

175 $$R_{rs}(\lambda) = 0.52 \times r_{rs}(\lambda) / (1 - 1.7 \times r_{rs}(\lambda)).$$ (8)

176 The water-leaving reflectance ρ_w in (1) is simply calculated from the R_{rs}.

177 $$\rho_w(\lambda) = \pi \times R_{rs}(\lambda)$$ (9)

178 We used the LMI scheme [42,43,44] to estimate IOPs. The scheme requires a_w, b_{bw}, and

179 model spectra, a_{ph}', a_{dg}' (absorption of detritus + CDOM), and b_{bp}', which is normalized at a

180 specific wavelength (442 nm was used in this study). We used a_w and b_{bw} values from [53,54]

181 weighted by the AVNIR-2 spectral response (shown in Table 3). Wavelength functions of a_{dg}

182 and b_{bp} were as follows.

183 $$a_{dg}(\lambda_b) = a_{dg0} \times a_{dg}(\lambda)'$$ (10)

184 $$b_{bp}(\lambda_b) = b_{bp0} \times b_{bp}(\lambda_b)'$$ (11)

185 where

186 $$a_{dg}(\lambda)' = \exp(S \times (\lambda - 442))$$ (12)

187 $$b_{bp}(\lambda)' = (\lambda /442)^Y$$ (13)

188 where a_{dg0} is a_{dg} at 442 nm, b_{bp0} is b_{bp} at 442 nm, S= −0.010 or −0.018, and Y= −1.4, 0, or +2. S

189 = −0.010 and Y = −1.4 were derived from the New Caledonia in situ measurements of a_{dg} and

190 b_{bp} respectively.

191   The inversion process was simplified to use only two IOP parameters, a_{pg} ($\equiv a_p + a_g \equiv$

192    $a_{ph} + a_{dg}$) and b_{bp}, and two AVNIR-2 bands, band 1 (463 nm) and band 2 (560 nm). We set the

193   a_{pg}' as follows.

194    $$a_{pg}(\lambda_b) = a_{pg0} \times a_{pg}(\lambda_b)' = a_{pg0} \times \{ (1- r_{pg}) \times a_{ph}(\lambda_b)' + r_{pg} \times a_{dg}(\lambda_b)' \} \tag{14}$$

195   where a_{pg0} is a_{pg} at 442 nm. The ratio of a_{ph} and a_{dg} at 442 nm, r_{pg}, was set to 0.52 / (1 + 0.52)

196   considering the normal conditions observed in the New Caledonia in situ data [32]. We can

197   estimate two parameters of IOPs, a_{pg0} and b_{bp0}, by the iteration processes of the IOP forward

198   calculation and LMI [42,43,44].

199   If we have an initial value of a_{pg0} and b_{bp0}, ρ_w can be calculated by (4)-(14). Using the ρ_w,

200   ρ_{ag} at 652 nm and 821 nm can be calculated using molecular scattering corrected reflectance

201   derived from satellite observation (ρ_{agw}) as:

202    $$\rho_{ag}(\lambda) = \rho_{agw}(\lambda) - \rho_w(\lambda) \tag{15}$$

203   where $\lambda = 652$ nm and 821 nm. Considering an approximation of Eq. (3), α can be calculated

204   by Eq. (16).

205    $$\alpha = \log(\rho_{ag}(652 \text{ nm}) / \rho_{ag}(821 \text{ nm})) / \log(652 \times c_{wl} / 821) \tag{16}$$

206   Then, ρ_w at 463 nm and 560 nm are calculated by Eqs. (3) and (15). Using the ρ_w at the two

207   visible bands, a_{pg0} and b_{bp0} can be calculated by the LMI [42,43,44].

208   The iteration process to derive the final value of a_{pg0} and b_{bp0} is shown in Fig. 2. The first

209   process aims to estimate α except for shallow areas (bathymetry<20m) where the bottom

210   reflectance can influence r_{rs}. The iteration was repeated to find optimal values of a_{pg0} and b_{bp0}

211   by minimizing the difference between b_{bp0} preset in Eq. (11) and b_{bp0} calculated by the

212   inversion matrix. The initial value of a_{pg0}' was set to 0.01, which does not affect the final a_{pg0}

213   estimates because a_{pg} is relatively small in the total a in red and NIR wavelengths. The sub-

214   process is repeated until $| a_{pg0} - a_{pg0}' | < 0.0001$ (practically less than four times in most pixels)

215   with revision of a_{pg0} and the search range of b_{bp0} ($b_{bp0}^{(max)}$) which is set by ρ_{ag} at 821 nm and

216   the extremely high $a_{pg0} = 20$ m^{-1}. After completing the first process, we smoothed α for each

217   0.1 deg $\times$ 0.1 deg area to reduce the AVNIR-2 sensor noise and extrapolate to the shallow

218   (<20m) areas where we did not estimate α in the first process. The second process derives ρ_{ag}

219   a_{pg}, b_{bp}, and R_{rs} for every 30-m grid using the same equations. We can derive IOPs and R_{rs} at

220   any wavelengths (AVNIR-2 bands at 463 nm and 560 nm and the wavelengths of the in situ

221   measurements at 442 nm and 555 nm) using the IOP spectra $a_{pg}(\lambda)$' and $b_{bp}(\lambda)$' (see section

222   2.5).

223   2.4   Chlorophyll-a estimation

224   Chlorophyll-a was estimated by regression of a_{pg}(442 nm) and the empirical blue/green as

225   follows:

226   $$\log_{10}(Chla) = 0.9706 + 1.1835 \times \log_{10}(a_{pg}(442 \text{ nm})) \tag{17}$$

227   $$\log_{10}(Chla) = 0.1464 - 1.7953\, r + 0.9718\, r^2 - 0.8319\, r^3 - 0.8073\, r^4 \tag{18}$$

228   where
229   $$r = \log_{10}(R_{rs}(463 \text{ nm}) / R_{rs}(560 \text{ nm})). \tag{19}$$

230   The relationship between *Chla* and a_{pg}(443 nm) was derived from a_{pg} and the fluorometric

231   chlorophyll-a data included in the bio-Optical Marine Algorithm Data set (NOMAD) [55] (Fig.

232   3). The MODIS OC2M-HI equation developed by the NASA Ocean Biology Processing Group

233 (OBPG) using the NOMAD database [6] was used for the two channel equation because

234 AVNIR-2 has only two channels in blue and green wavelengths.

2.5 In situ bio-optical measurements

236   Field measurements of the two IOPs, the absorption coefficient, a, and the backscattering

237 coefficient, b_b, were obtained at stations in the southwest part of the lagoon (Fig. 1) during

238 various seasons from 2006 to 2010. The b_b was measured with a Hydroscat-6 profiler (H6:

239 HobiLabs, wavebands (λ) centered at 442, 488, 510, 550, 620 and 670 nm with a bandwidth of

240 10 nm for the 442–550 nm bands and 20 nm for the 620 and 670 nm bands) [19,27]. The

241 particulate back-scattering coefficient, $b_{bp}(\lambda)$, was calculated by subtracting from $b_b(\lambda)$ the

242 theoretical "pure water spectrum", $b_{bw}(\lambda)$ (calculated as $b_{bw}(\lambda) = 0.5 \times b_w(\lambda)$) [51]. The

243 particulate absorption coefficient, $a_p(\lambda)$, was measured with the filter-pad technique [56] using

244 water samples filtered onto 25-mm GF/F Whatman filters. For pigments, the filters were

245 dipped in 5.4 ml 100% acetone (final concentration 90% acetone taking into account water

246 retention by the filter, e.g., 0.621 ± 0.034 ml) and ground with the freshly broken end of a glass

247 rod for chlorophyll and phaeopigment extraction [57]. For comparison with the satellite-

248 estimated *Chla*, we used the sum of chlorophyll a and divinyl chlorophyll a, *Chla* (in mg m^{-3}),

249 as measured by spectrofluorometry, and well correlated with fluorometry in the Caledonian

250 lagoon [15,27].

251   For the LMI, we prepared the model spectra of a_{pg} and b_{bp} optimized for the New

252 Caledonia in situ samples (six samples of a_{ph} and a_{dg} in 2003, and 112 samples of b_{bp} in 2006-

253 2010). The samples of a_{ph} and a_{dg} were distributed around the lagoon of the southeast New

254 Caledonia, but not near bays of the mainland. The spectral shape a_{dg}' and b_{bp}' (relative values

255   from λ=442 nm) were modeled by Eqs. (12) and (13) respectively. The model spectra from the

256   averages of the New Caledonia measurements were used as the standard in sensitivity tests

257   described below.

258   We tested the sensitivity of different sets of model spectra: (A) a_{pg}' and b_{bp}' from the New

259   Caledonia measurements (e.g., same as the above); (B) same as (A) but a_{ph}' from a

260   picoplankton spectra [58]; (c) same as (A) except for a_{ph}' from a microplankton spectra [58];

261   (D) same as (A) except for a_{dg}' with $S = -0.018$; (E) same as (A) except for b_{bp}' with $Y = 0.0$;

262   and (F) same as (A) except for b_{bp}' with $Y = -2.0$ (Fig. 4). These a_{ph}' spectra are listed in Table

263   3.

264   ## 2.6 Correction of sea floor reflection

265   The R_{rs} and IOP estimation might be influenced by bottom reflectance especially in low

266   absorption and shallow areas, such as site G003 near the barrier reef (11 meters depth, bottom

267   composed of white sands). r_{rs} in shallow areas was approximated by the following equation

268   from [59]:

269
$$r_{rs} \sim r_{rs}^{dp} \times [1 - \exp\{ -\kappa H \times (1 / \cos\theta_{0w} + D_u^C / \cos\theta_w) \}]$$

270
$$+ \rho_b / \pi \times \exp\{ -\kappa H \times (1 / \cos\theta_{0w} + D_u^B / \cos\theta_w) \} \tag{20}$$

271   where ρ_b is the bottom albedo, H is the bottom depth, θ_{0w} is the subsurface solar zenith angle,

272   θ_w is the subsurface viewing angle from nadir ($\theta_w = \sin^{-1}(1 / 1.34 \times \sin \theta_a)$, θ_a is the above-

273   surface angle), r_{rs}^{dp} is the remote-sensing reflectance for optically deep water, and κ is the

274   attenuation coefficient ($\kappa(\lambda) = a(\lambda) + b_b(\lambda)$). D_u^C and D_u^B are optical path-elongation factors

275   for scattered photons from the water column and bottom respectively, which are described by

276   functions of $u(\lambda)$ following [59].

277   Because ρ_b is unknown at each image grid in this study, we used a ρ_b spectrum of coral

278   sand shown by Fig. 6 of [60] ($\rho_b = 0.33$ and 0.47 at 442nm and 555nm respectively). The

279   similar ρ_b spectra of the sandy sea bottom were reported around the coral reef system by

280   [61,62]. We use H compiled in [12] (Fig. 5). Attenuation coefficient, $\kappa(\lambda)$, is iteratively

281   calculated through the IOP estimation described in section 2.3 by changing H from enough

282   deep depth (1000m) to the actual sea-floor depth gradually. Such an approach has been used to

283   retrieve bathymetry [36].

284   ## 2.7   MODIS ocean color products

285   NASA OBPG Aqua MODIS products, R_{rs} at 443 nm, R_{rs} at 555 nm, and *Chla* (processing

286   version 2009.1) [6], were used for the comparison to our results. The global accuracies of the

287   MODIS data set, reported as the median absolute percent differences of normalized water-

288   leaving radiance (L_{wn}) at 443 nm, L_{wn} at 555 nm, and *Chla* from global in situ observations, are

289   18%, 17%, and 37% respectively [6,63]. We selected clear MODIS scenes ± 1 day from

290   AVNIR-2 observations or between the AVNIR-2 and in situ observation dates.

291   **3. RESULTS**

292   ### 3.1 R_{rs} and ρ_{ag}

293   Figure 6 shows results of the ρ_{agw} (463 nm), ρ_{ag} (463 nm), α, ρ_w (463 nm) without bottom

294   correction, and ρ_w (463 nm) with bottom correction on 17 Nov. 2008 and 3 Sep. 2009. On 17

295   Nov. 2008, the area was covered by sunglint (brighter on the right side in Figs. 6a and 6b). ρ_{ag}

296   (Fig. 6b) showed small-scale structures of the surface reflection caused by the winds and

297 geographical features. α (Figs. 6c and 6h) was smoothed in each 0.1 deg × 0.1 deg grid after

298 the first process ((a) in Fig. 2). The estimated ρ_w (Fig. 6d) was very smooth offshore and

299 showed fine structures inside the lagoon. On 3 Sep. 2009, aerosol with small clouds extended

300 northwest to southeast over the area (Fig. 6g). The aerosol pattern was removed effectively in

301 the ρ_w image (Fig. 6i) by subtracting ρ_{ag} (Fig. 6g) from ρ_{agw} (Fig. 6f). High reflectance areas

302 remained inside the lagoon with a dark area along the outside of the barrier reef.

303 The comparison between AVNIR R_{rs} and MODIS R_{rs} at 442nm (or 443 nm) and 555 nm is

304 shown in Fig. 7. AVNIR-2 R_{rs} at 555nm appears slightly higher, but the results are closely

305 correlated (0.77 and 0.54 at 442 nm and 555 nm, respectively, and the Root Mean Square

306 Difference (RMSD) was about 40% and 63% of the average R_{rs} for AVNIR-2 and MODIS,

307 respectively) except for some samples at the shallow stations (*e.g.*, B50 and B03). An outlier at

308 station G003 in Fig 7a (AVNIR-2 R_{rs} at 442 nm is about 0.03) seemed to be influenced by

309 cloud edge in the AVNIR-2 image on 31 Jul. 2007.

310 Figures 6e and 6j show the AVNIR-2 ρ_w at 463nm with the correction of bottom

311 reflectance. The correction decreases ρ_w inside of the lagoon (*e.g.*, at stations M33 and G003)

312 and reduces the pattern of the bathymetry (seen Fig. 5) in most areas in the ρ_w images.

313 However, it seems to cause overcorrection in some areas, *e.g.*, around the islands and the

314 barrier reef.

315 3.2 a_{pg} and b_{bp}

316 Figures 8a and 8b shows a_{pg} at 442nm and b_{bp} at 555nm without the bottom correction

317 (using model spectra (A) in Table 4). a_{pg} was high along the coast and in bays near the main

318 land. On the other hand, b_{bp} was high inside the lagoon especially at shallow bottom areas (e.g.,

319   G003). Scatter plots between the in situ ($a_p \times 1.52$) and the AVNIR-2 a_{pg} and b_{bp} estimates are

320   shown in Figs. 9a and 9b. They show that AVNIR-2 a_{pg} is well correlated with in situ values

321   for a_{pg} (r = 0.91 in Fig. 9a) even though the factor 1.52 may vary with changing proportions of

322   a_p or a_g in $a_{pg} = a_p + a_g$. AVNIR-2 b_{bp} showed a high correlation coefficient (about 0.94 at 555

323   nm), but some values of b_{bp} were higher than the in situ b_{bp}. The overestimated samples were

324   found in shallow areas (3.6 m, 6 m, 5m, and 11 m at stations B50, B03, Ile aux Canards and

325   G003 respectively).

326   Figures 8c and 8d show a_{pg} and b_{bp} with the bottom reflectance correction on 3 Sep 2009.

327   The correction decreased a_{pg} and b_{bp} in the lagoon areas. The comparison to the in-situ

328   observations (Figs. 9c and 9d) showed that the correction improved the agreement especially at

329   stations M33, Ile aux Canards, and G003 where the bottom depth is shallow and a_{pg} is

330   relatively low. The AVNIR-2 a_{pg} was still higher than the in-situ a_{pg} at stations B50 and B03

331   around the Boulari Bay. Bias of a_{pg} (b_{bp}) were improved from 0.188 to 0.118 (from 0.023 to

332   0.015), and RMSD of a_{pg} (b_{bp}) from 0.489 to 0.290 (from 0.042 to 0.025) by the bottom

333   correction.

334   Table 4 shows the results for the fifteen match-ups by using different spectra of a_{pg} and b_{bp}.

335   Superscripts − and + show results with smaller or larger bias or RMSD (statistically

336   significance level of 95%) than ones by the model spectrum (A). The results depended on the

337   model spectra significantly, and the model (D) brought the smallest RMSD of both a_{pg} and b_{bp}

338   with the bottom reflectance correction. Note that the microplankton for a_{ph} [58] gives larger

339   RMSD than the measured around New Caledonia. Similarly, a slope of $Y = -2$ is too different

340   from those measured and would not allow a proper retrieval of IOPs from AVNIR-2. Figures

341   9e-9h show the scatter plots by the model spectrum (D). RMSDs of a_{pg} and b_{bp} are significantly

342   decreased (especially stations B50 and B03) by the optimal model spectrum.

343   3.3 Chlorophyll-a concentration

344   Figures 10 and 11 show the comparison among *Chla* estimated from a_{pg} (by the optimal

345   model (D)), *Chla* calculated by OC2M-HI (using R_{rs} by AVNIR-2), and the MODIS standard

346   (OC3M) 1-km *Chla*. *Chla* estimated from a_{pg} (Figs. 10a and 11a) was slightly smaller than

347   *Chla* determined by other algorithms in the lagoon areas (*e.g.*, sites B08 and Ile aux Canards in

348   Figs. 10 and 11). The AVNIR-2 OC2M-HI *Chla* was larger than indicated by the in situ data

349   and similar to the MODIS standard value in the lagoon (see around sites M33 and G003 in Figs.

350   10b, 10e, and Figs. 11b and 11e). The scatter plots show that *Chla* from a_{pg} provides the best

351   agreement among the three methods in the lagoon (RMSD=0.47, 0.61, and 0.60 in Figs. 10a,

352   10b, and 10e). The MODIS data at stations M33 and GD10 were scattered because they were

353   too near the coast or the lagoon islands compared to the 1-km resolution products.

354   Figures 11c and 11d show results with the bottom correction. OC2M-HI *Chla* (Fig. 11d)

355   was calculated by R_{rs} from $r_{rs}{}^{dp}$ (Eq. (8)). Usual high biases of a_{pg} and b_{bp} in the shallow areas

356   (B50, B03, and Ile aux Canards) around lagoon islands were decreased by the correction (Figs.

357   8c and 8d). It reduced overestimate of *Chla* by both a_{pg} and OC2 schemes, and improved the

358   agreement with the in-situ matchups inside the lagoon (Figs. 10c and 10d).

4. DISCUSSION

4.1 a_{pg} and b_{bp} spectra

Agreement with in situ data was dependent on spectra of a_{pg} and b_{bp} (Table 4). For example, the a_{ph} spectrum of microplankton [58] (model C) and b_{bp} spectrum of Y=−2.0 (F) caused worse results than the spectrum modeled from New Caledonia in situ measurements (A) (Table 4). The agreement may be improved further if we optimize the spectra to more specific water types, *e.g.*, bays near the main land, middle-lagoon waters, and waters outside of the barrier reef (*e.g.*, open ocean). For example, modification of spectral slope of a_{dg} improved the IOP estimate especially around the Boulari Bay (model (D) in Fig. 9). The accuracies of the best results (r=0.91 and r=0.75 in Figs. 9g and 9h respectively) were better than ones by Quasi-Analytical Algorithm (QAA) [52,64] by using 1km MODIS Aqua Rrs data (r=0.84 and 0.72 for a_{pg} 443nm and b_{bp} 555nm respectively (Figures of QAA results are not shown here).

Such an optimization with the best-candidate spectra can be a useful way to obtain locally-optimized environmental monitoring from satellite observations with theoretical understanding of the local optical environment.

This study cannot determine spectral models such as the ratio between a_p and a_g (or a_{ph} and a_{dg}), because AVNIR-2 has only two channels in the blue and green wavelengths. More bands at 250 m to 300 m of spatial resolution from sensors such as SGLI and OLCI may be able to improve the discrimination of the IOPs.

The IOP retrieval schemes have been developed for observations by narrow (about 10-20nm) band-width sensors, estimates of absorption coefficients by the wide band can cause errors reaching about 20% [65] by the QAA [52,64] through the integration of the IOP spectra

381   in the band wavelengths. Our estimates rely on relatively wide bands (about 90nm) of AVNIR-

382   2. We confirmed our retrieval of a_{pg} by the LMI can change about 20% (mostly overestimated)

383   using simulated *Rrs* from our in-situ a_{pg} and b_{bp}. The error is still much smaller than the error

384   due to difference of the model IOP spectra, however, it will need to be considered for more

385   precise estimate in the future.

386   ## 4.2 Aerosol and sea surface reflection estimation

387   Most of the iteration schemes for the atmospheric correction use the relationship between

388   NIR R_{rs} and *Chla*. This study uses the relationships among a_{pg}, b_{bp}, ρ_{ag}, and α based on the

389   convergence of b_{bp}. This scheme can avoid negative IOPs by tuning the aerosol parameters α

390   and ρ_{ag} in the iteration process. Another merit of this aerosol estimation is the fast processing

391   time (2-3 minutes for our study area (2001×1334 pixels) by a wide-use PC Linux machine)

392   because it does not require time to access the aerosol look-up table that is used in the standard

393   ocean color atmospheric correction algorithms.

394   The New Caledonia lagoon area has a relatively clear atmosphere compared to coasts in the

395   northern hemisphere, such as the Asian coasts. This scheme does not consider absorptive

396   aerosols that cannot be described by the simple Eq. (3). For more complex atmosphere

397   (aerosol) conditions, more bands may be necessary than the two that were used here for the

398   aerosol characterization (this study used 652 nm and 821 nm). If the sensor has lower noise and

399   SWIR bands (e.g., MODIS 500 m bands and SGLI 250m band), we may be able to estimate α

400   at each pixel and obtain more realistic measurements of α and ρ_{ag}. However, the absorptive

401   aerosol correction may still be difficult using the simple Eq. (3).

402   4.3   The bottom effect

403   AVNIR-2 b_{bp} seemed to be influenced by the bottom reflectance. Bottom sands can be seen

404   from satellite if bathymetry is shallow. For example, the bottom depth of the station G003 is 11

405   m with a relatively low a_{pg}. Agreement between AVNIR-2 IOPs and in situ IOPs were

406   improved by considering the bottom reflectance generally, but they seemed to be overcorrected

407   in some areas around the islands and along the barrier reef (Fig 6j). They are supposed to be

408   influenced by coverage of live corals or sediment from the land, which may cause a different

409   spectrum of the bottom reflectance from the coral sand reflectance [60,61,62]. This indicates

410   that our IOP estimation could be improved if the precise bottom depth and real bottom

411   reflectance are used [36].

412   4.4   Cloud shadow and adjacent scattering

413   For the 10-m resolution data, it is important to consider cloud shadow and sea surface

414   reflection of scattered light from the cloud bottom. Identification of clouds around the coast

415   (including over the land) and geometric calculation considering the cloud height are required.

416   In addition, the clouds and land area can influence the coastal ocean color estimation, which is

417   known as the adjacent effect [66]. The influence of the cloud shadow seemed to affect b_{bp}, but

418   not a_{pg} as observed in the southeastern part of Fig. 8. Further study is needed to determine b_{bp}

419   in the absence of the influence of the cloud effects.

420   **5. CONCLUSION**

421   This study investigated the correction of atmospheric scattering and sea surface reflection

422   in the southwest region of the New Caledonia lagoon using AVNIR-2 images, which have four

423   bands from visible to NIR wavelengths with 10-m resolution (our processing was conducted

424   after averaging for 30-m (3×3) grids). We applied corrections for gas absorption, molecule

425   scattering, and $\rho_a + \rho_g$ using the iteration scheme for converging b_{bp} through IOPs from visible

426   bands. This scheme was able to correct fine structure patterns of the $\rho_a + \rho_g$ successfully. The

427   AVNIR-2-estimated R_{rs} agreed well with the MODIS R_{rs} (root-mean square difference /

428   average of R_{rs} at 443 nm = 40%). Future projects, e.g., the Global Change Observation Mission

429   (GCOM), using the Second-generation Global Imager (SGLI) and the Sentinel-3 Ocean and

430   Land Colour Imager (OLCI), will have finer (250 m - 300 m) spatial resolution aiming for

431   coastal monitoring with a swath of more than 1150 km. These missions will require a

432   correction of the surface reflection with high spatial resolution and a reduction of masked areas

433   in order to increase the observation frequency in the coastal areas.

434   With the bottom correction, the AVNIR-2-estimated IOPs agreed well with in situ IOP

435   measurements (correlation coefficients were more than 0.9). Overcorrection appeared in the

436   muddy bays and along the barrier reef, and it suggested that a constant bottom reflectance was

437   not applicable in these areas.

438   This study showed that the AVNIR-2-estimated *Chla* from the a_{pg} regression scheme in the

439   lagoon area does not show the overestimation observed with the blue / green R_{rs} ratio. This

440   also confirms that the relationship between *Chla* and a_{pg} in the lagoon area is not different from

441   the a_{pg}-*Chla* relationship of the NOMAD database as already shown in [27]. The NOMAD

442   relationship cannot be used in bays (*e.g.*, B50), where the a_{pg}-*Chla* relationship is disturbed by

443   absorbing mineral particles and irregular a_g due to river discharge.

444   Our atmospheric correction and IOP estimation scheme which requires only four bands in

445   the visible and NIR wavelengths can be applied to other satellite sensors, such as the MODIS

446   500-m bands, and other multi-band sensors, such as SGLI 250-m bands. The performance

447   depends on the candidate spectra of IOPs based on in situ measurements (and aerosols) in the

448   target areas. This reinforces the need to construct databases of the various spectra of IOPs and

449   aerosols in various regions through international collaboration to develop globally applicable

450   approaches. The target of this study is not to make a fixed algorithm, but demonstrate the

451   method to make local optimal estimate of the IOPs and *Chla*. So, the algorithm should not be

452   applied elsewhere without a similar effort *i.e.*, preparation of the candidate spectra for the

453   target areas.

464

465   **APPENDIX:**

466   **Calculation of TOA reflectance with gaseous absorption correction**

467     $\rho_t(b) = L_{avnir2}(b) / f_{vc}(b) \times \pi \times d^2 / F_0(b) / \cos(\theta_{sun}) / t_{oz} / t_{wv} / t_{O2}$ (A1)

468   where $t_{oz} = \exp(-k_{oz}(b) \times (oz - 343.8) \times pl)$ (A2)

469         $t_{wv} = \exp(-\{ k_{wv}(b) \times (ptw - 14.19) \times pl + k_{wv2}(b) \times ((ptw \times pl)^2 - (14.19 \times pl)^2) \})$ (A3)

470         $t_{O2} = \exp(-k_{O2}(b) \times (prs - 1013.25) \times 0.2095 \times pl)$ (A4)

471         $pl = 1 / \cos(\theta_{sun}) + 1 / \cos(\theta_{sat})$ (A5)

472   L_{avnir2} is the AVNIR-2-observed radiance [W/m^2/µm/sr], b represents the AVNIR-2 spectral

473   bands, f_{vc} is the vicarious calibration factor defined as ratio of AVNIR-2 radiance to radiance

474   simulated by MODIS observation, d is the sun-earth distance [AU], F_0 is the solar irradiance at

475   1 AU [67], θ_{sun} is the solar zenith angle [rad], θ_{sat} is the satellite zenith angle [rad], oz is the

476   column ozone [DU], ptw is the column water vapor [mm], and prs is the sea-level pressure

477   [hPa]. The gas absorption coefficients k_{oz}, k_{wv} and k_{O2} were calculated by MODTRAN 4 [68]

478   considering the spectral response of the AVNIR-2 bands (Table 2). We used ptw and prs from

479   the National Centers for Environmental Prediction (NCEP) and oz from the Ozone Monitoring

480   Instrument (OMI), which is distributed by Goddard Space Flight Center.

481   **REFERENCES**

482   1.   R. Frouin, M. Schwindling, and P. Y. Deschamps, "Spectral reflectance of sea foam in the

483   visible and near infrared: in situ measurements and remote sensing implications," *Journal*

484   *of Geophysical Research, 101*, 14361-14371 (1996).

485   2.   K. D. Moore, K. J.Voss, and H. R. Gordon, "Spectral reflectance of whitecaps: their

486   contribution to water-leaving radiance", *Journal of Geophysical Research,* 105, 6493-6499

487   (2000).

488 3. J.-M. Nicolas, P.-Y. Deschamps, and R. Frouin, "Spectral Reflectance of Oceanic

489   Whitecaps in the Visible and near Infrared: Aircraft Measurements Over Open Ocean,"

490   *Geophysical Reearch Letter*, *28 (23)*, 4445-4448 (2001).

491 4. C. Cox, and W. Munk, "Measurements of the roughness of the sea surface from

492   photographs of the sun's glitter," *Journal of the Optical Society Of America.*, 44, 838-850

493   (1954).

494 5. M. Wang, and S.W. Bailey, "Correction of sun glint contamination on the SeaWiFS ocean

495   and atmosphere products," *Applied Optics,* 40, 4790-4798 (2001).

496 6. G.C. Feldman, "The OC2 algorithm for MODIS," Seadas Forum, NASA-GSFC, NASA

497   OceanColor webpage http://oceancolor.gsfc.nasa.gov/REPROCESSING/R2009/.

498 7. E. Hochberg, S. Andrefouet, and M. Tyler, "Sea Surface Correction of High Spatial

499   Resolution Ikonos Images to Improve Bottom Mapping in Near-Shore Environments,"

500   *IEEE Trans. Geosci. Remote Sens.*, 41, 1724-1729 (2003).

501 8. J. A. Goodman, Z-P. Lee, and S. L. Ustin, "Influence of Atmospheric and Sea-Surface

502   Corrections on Retrieval of Bottom Depth and Reflectance Using a Semi-Analytical

503   Model: A Case Study in Kaneohe Bay, Hawaii," *Appl. Optics*, 47, F1-F11 (2008).

504 9. H. Murakami, and R. Frouin, "Correction of sea surface reflection in the coastal area,"

505   *Proc. SPIE* Vol. 7150-4, Remote Sensing of Inland, Coastal, and Oceanic Waters edited by

506   R. Frouin, *Proc. SPIE Asia-Pacific Remote Sensing*, 17-21 November 2008, Nouméa, New

507   Caledonia (2008).

508 10. R. Fichez, L. Breau, C. Chevillon, S. Chifflet, P. Douillet, V. Faure, J.M. Fernandez, P.

509   Gérard, L. Hédouin, A. Lapetite, S. Ouillon, O. Pringault, and J.P. Torréton, "Origine,

510   transport et devenir des apports naturels et anthropiques dans le lagon sud-ouest de

511   Nouvelle-Calédonie," *Journal de la Société des Océanistes*, 126-127, 41-58 (2008).

512 11. R. Fichez, S. Chifflet, P. Douillet, P. Gerard, F. Gutierrez, A. Jouon, S. Ouillon, and C.

513   Grenz, "Biogeochemical typology and temporal variability of lagoon waters in a coral reef

514   ecosystem subject to terrigeneous and anthropogenic inputs (New Caledonia)," *Marine*

515   *Pollution Bulletin,* 61, 7-12, 309-322 (2010).

516 12. S.Ouillon, P.Douillet, J.P. Lefebvre, R. Le Gendre, A. Jouon, P. Bonneton, J.M. Fernandez,

517   C. Chevillon, O. Magand, J. Lefevre, P. Le Hir, R. Laganier, F. Dumas, P. Marchesiello, A.

518   Bel Madani, S. Andrefouet, J.Y. Panche, and R. Fichez, "Circulation and suspended

519   sediment transport in a coral reef lagoon: the southwest lagoon of New Caledonia," *Marine*

520   *Pollution Bulletin,* 61, 7-12, 269-296 (2010).

521 13. J.Lefèvre, P. C. Marchesiello, N. C. Jourdain, C. Menkes, and A. Leroy, "Weather

522   regimes and orographic circulation around New Caledonia," *Marine Pollution Bulletin*, 61,

523   413-431 (2010).

524 14. R.Fuchs, C. Dupouy, P. Douillet, F. Dumas, M. Caillaud, A. Mangin, and C. Pinazo,

525   "Modelling the impact of a La Niña event on a South West Pacific Lagoon," *Marine*

526   *Pollution Bulletin* (2012) *in press*.

527 15. J. Neveux, M.M.B. Tenorio, S. Jacquet, J.-P. Torreton, P. Douillet, S. Ouillon, and C.

528   Dupouy, "Chlorophylls and phycoerythrins as markers of environmental forcings

529   including cyclone Erica effect (March 2003) on phytoplankton in the southwest lagoon of

530   New Caledonia and oceanic adjacent area," *International J. Oceanogr., Article ID 23251,*

531   doi:10.1155/2009/232513 (2009).

532   16. J.P. Torréton, E. Rochelle-Newall, O. Pringault, S. Jacquet, V. Faure, E. Briand,

533   "Variability of primary and bacterial production in a coral reef lagoon (New Caledonia),"

534   *Mar Pollut Bull*, **61**, 335-348 (2010).

535   17. C. Dupouy, G. Dirberg, J. Neveux, M. Tenorio, and A. Le Bouteiller, "The contribution of

536   T*richodesmium* to inherent optical properties of a tropical oligotrophic archipelago," in:

537   Conference CD-ROM ''OCEAN OPTICS XVII", 26 October–3 November 2004,

538   Fremantle, Australia, 3pp (2004).

539   18. C. Dupouy, D. Benielli-Gary, Y. Dandonneau, J. Neveux, G. Dirberg, and T. Westberry,

540   "On the feasibility of detecting *Trichodesmium* blooms with SeaWiFS in the South

541   Western Tropical Pacific," Remote Sensing of Inland, Coastal, and Oceanic Waters.

542   *Proceedings of SPIE,* vol. 7150. SPIE, Bellingham, WA [7150 37] 715010, 9pp (2008).

543   19. C. Dupouy, J. Neveux, G. Dirberg, M.M.B. Tenorio, R. Rottgers, and S. Ouillon, "Bio-

544   optical properties of marine cyanobacteria *Trichodesmium*, spp.," *Journal of Applied*

545   *Remote Sens.* 2, 023503 (2008).

546   20. C. Dupouy, D. Benielli-Gary, J. Neveux, Y. Dandonneau, and T. Westberry, "A new

547   algorithm for detecting Trichodesmium surface blooms in the South Western Tropical

548   Pacific," *Biogeosciences*, 8, 1-17 (2011).

549   21. A. Ganachaud, A. Vega, M. Rodier, C. Dupouy, C. Maes, P. Marchesiello, G. Eldin, K.

550   Ridgway, and R. Le Borgne, "Observed impact of upwelling on water properties and

551   biological activity off the southwest coast of New Caledonia," *Marine Pollution Bulletin,*

552   61, 449-464 (2010).

553   22. J. Neveux, J.-P. Lefebvre, R. Le Gendre, C. Dupouy, F. Gallois, C. Courties, P. Gerard, S.

554   Ouillon, and J.M. Fernandez, "Phytoplankton dynamics in New-Caledonian lagoon during

555   a southeast trade winds event," *Journal Marine Systems*, 82, 230-244, doi:10.1016/

556   j.jmarsys.2010.05.010 (2010).

557 23. C. Dupouy, A. Minghelli-Roman, M. Despinoy, R. Röttgers, J. Neveux, S. Ouillon, C.

558   Pinazo, and M. Petit, "MODIS/Aqua chlorophyll monitoring of the New Caledonia

559   lagoon: the VALHYBIO project," in *Proceedings of SPIE*, Vol. 7150 (SPIE, Bellingham,

560   WA, 2008) [7150 41] 715014, 8 pp (2008).

561 24. R. Fuchs, C. Pinazo, P. Douillet, C. Dupouy, and V. Faure, "New Caledonia Surface

562   lagoon chlorophyll modeling as coastal reef area health indicator," in "*Remote sensing of*

563   *the coastal ocean, land, and atmosphere environment*" edited by Robert J. Frouin, Proc.

564   SPIE Vol. AE103 (SPIE, Bellingham, WA, 2010) [7858 20], 9 pp (2010).

565 25. M. Babin, D. Stramski, G.M. Ferrari, H. Claustre, A. Bricaud, and G. Obolenski,

566   "Variations in the light absorption coefficients of phytoplankton, non-algal particles, and

567   dissolved organic matter in coastal waters around Europe," *Journal of Geophysical*

568   *Research,* 108. doi:10.1029/2001JC000882 (2003).

569 26. C.M. Hu, Z.Q. Chen, T.D. Clayton, P. Swarzenski, J.C. Brock, and F.E. Muller-Karger,

570   "Assessment of estuarine water-quality indicators using MODIS medium resolution bands:

571   initial results from Tampa Bay, FL.," *Remote Sensing of Environment,* 93, 423–441 (2004).

572 27. C. Dupouy, J. Neveux, S. Ouillon, R. Frouin, H. Murakami, S. Hochard, and G. Dirberg,

573   "Inherent optical properties and satellite retrieval of chlorophyll concentration in the

574   lagoon and open ocean waters of New Caledonia," *Marine Pollution Bulletin 61*, 503–518,

575   doi:10.1016/j.marpolbul.2010.06.039 (2010).

576   28. J.G. Acker, A. Vasilkov, D. Nadeau, and N. Kuring, "Use of SeaWiFS ocean color data to

577   estimate neritic sediment mass transport from carbonate platforms for two hurricane-

578   forced events," *Coral Reefs,* 23, 39–47 (2004).

579   29. D. Blondeau-Patissier, V.E. Brando, K. Oubelkheir, A.G. Dekker, L.A. Clementson, and P.

580   Daniel, "Bio-optical variability of the absorption and scattering properties of the

581   Queensland inshore and reef waters, Australia," *Journal of Geophysical Research,* 114,

582   C05003,doi:10.1029/2008JC005039 (2009).

583   30. K. Oubelkheir, L.A. Clementson, I.T. Webster, P.W. Ford, A.G. Dekker, L.C. Radke, and

584   P.Daniel, "Using inherent optical properties to investigate biogeochemical dynamics in a

585   tropical macrotidal coastal system," *Journal of Geophysical Research,* 111, C07021

586   doi:10.1029/2005JC003113 (2006).

587   31. S. Ouillon, P. Douillet, A. Petrenko, J. Neveux, C. Dupouy, J.-M. Froidefond, S.

588   Andréfouët, and A. Muñoz-Caravaca, "Optical Algorithms at Satellite Wavelengths for

589   Total Suspended Matter in Tropical Coastal Waters," *Sensors,* 8, 4165-4185; doi:

590   10.3390/s8074165 (2008).

591   32. C. Dupouy, and R. Roettgers, "Absorption by different components during a high

592   freshwater event of the 2008 La Nina episode in a tropical lagoon," Poster Session "Bio-

593   optics and biogeochemistry", *Ocean Optics XX*, Anchorage (Alaska), 25-30 September

594   2010 (2010).

595   33. Z-P. Lee, K.L. Carder, R.F. Chen, and T.G. Peacock, "Properties of the water column and

596   bottom derived from Airborne Visible Infrared Imaging Spectrometer (AVIRIS) data,"

597   *Journal of Geophysical Research,* 106, 11639–11651 (2001).

598   34. J.P. Cannizaro, and K.L. Carder, "Estimating chlorophyll a concentrations from remote-

599   sensing reflectance in optically shallow waters," *Remote Sensing of Environment,* 101, 13–

600   24 (2006).

601   35. A. Minghelli-Roman, L. Polidori, S. Mathieu-Blanc, L. Loubersac, and F. Cauneau,

602   "Bathymetric estimation using MeRIS images in coastal sea waters," *IEEE Transactions*

603   *Geosciences Remote Sensing,* 4, 274–277 (2007).

604   36. A. Minghelli-Roman, C. Dupouy, C. Chevillon, P. Douillet, "Bathymetry retrieval and sea

605   bed mapping in the lagoon of New Caledonia with MeRIS images," in *Proceedings SPIE,*

606   7858 (SPIE, Bellingham, WA, 2010) [78580Y (Nov. 3, 2010)], 7 pp., doi:

607   10.1117/12.870729 (2010).

608   37. S. Andréfouët, M. J. Costello, M. Rast, and S. Sathyendranath, "Preface: Earth

609   observations for marine and coastal biodiversity and ecosystems," *Remote Sensing of*

610   *Environment*, 112, 3297–3299 (2008).

611   38. C. Dupouy, T. Savranski, J. Lefevre, M. Despinoy, M. Mangeas, R. Fuchs, S. Ouillon, and

612   M. Petit, "Monitoring chlorophyll of the South West Tropical Pacific," Communication at

613   the 34th International Symposium on Remote Sensing of Environment, Sydney, 10-14

614   April 2011 (2011).

615   39. C. Dupouy, G. Wattelez, R. Fuchs, J. Lefèvre, M. Mangeas, H. Murakami, and R. Frouin,

616   "The colour of the Coral Sea," *In Proceedings of the 12th International Coral Reef*

617   *Symposium, 18E– The future of the Coral Sea reefs and sea mounts, Cairns, Australia, 9-*

618   13 July 2012, ICRS2012_18E-2 (2012).

619   40. T. Tadono, M. Shimada, H. Murakami, T. Hashimoto, J. Takaku, A. Mukaida, and S.

620   Kawamoto, "Initial results of calibration and validation for PRISM and AVNIR-2," *Asian*

621   *Journal of Geoinformatics,* 6, 4, 11–20 (2006).

622   41. H. Murakami, T. Tadono, H. Imai, J. Nieke, and M. Shimada, "Improvement of AVNIR-2

623   radiometric calibration by comparison of cross-calibration and on-board lamp calibration,"

624   *IEEE TGRS, 47, 12, pp. 4051-4059* (2009).

625   42. F.E. Hoge, and P.E. Lyon, "Satellite retrieval of inherent optical properties by linear

626   matrix inversion of oceanic radiance models: an analysis of model and radiance

627   measurement errors," *Journal of Geophysical Research,* 101, 16631-16648 (1996).

628   43. F.E. Hoge, and P.E. Lyon, "Spectral parameters of inherent optical property models:

629   Methods for satellite retrieval by matrix inversion of an oceanic radiance model," *Applied*

630   *Optics, 38*, 1657-1662 (1999).

631   44. P. Lyon, and F. Hoge, "The Linear Matrix Inversion Algorithm," *Chap. 7 of IOCCG*

632   *Report Number **5,*** Remote Sensing of Inherent Optical Properties: Fundamentals, Tests of

633   Algorithms, and Applications, Ed. by Z. Lee (2006).

634   45. Y. Ota, A. Higurashi, T. Nakajima, and T. Yokota, "Matrix formulations of radiative

635   transfer including the polarization effect in a coupled atmosphere-ocean system," *Journal*

636   *of Quantitative Spectroscopy and Radiative Transfer*, Vol. 111-6, 878-894 (2010).

637   46. T. Nakajima, and M. Tanaka, "Matrix formulation for the transfer of solar radiation in a

638   plane-parallel scattering atmosphere," *J. Quantitative Spectroscopic Radiative Transfer,* 35,

639   13-21 (1986).

640   47. T. Nakajima, and M. Tanaka, "Algorithms for radiative intensity calculations in moderately thick atmospheres using a truncation approximation," *Journal of Quantitative Spectroscopic Radiative Transfer,* 40, 51-69 (1988).

643   48. K. Stamnes, S.-C. Tsay, W. Wiscombe, and K. Jayaweera, "Numerically stable algorithm for discrete-ordinate-method radiative transfer in multiple scattering and emitting layered media," *Applied Optics,* 27, 2502-2509 (1988).

646   49. R. Frouin, P-Y. Deschanmps, L. Gross-Colzy, H. Murakami, and T. Y. Nakajima, "Retrieval of Chlorophyll-a Concentration via Linear Combination of ADEOS-II Global Imager Data," *Journal of Oceanography*, 62, 331-337 (2006).

649   50. R. Zaneveld, A. Barnard, and Z-P. Lee, "Why area Inherent Optical Properties Needed in Ocean-Colour Remote Sensing?," *Chap. 1 of IOCCG Report Number* 5, Remote Sensing of Inherent Optical Properties: Fundamentals, Tests of Algorithms, and Applications, Ed. by Z. Lee (2006).

653   51. H.R. Gordon, O.B. Brown, R.H. Evans, J.W. Brown, R.C. Smith, K.S. Baker, and D.K. Clark, "A semi-analytic radiance model of ocean color," *Journal of Geophysical Research,* 93 (D9), 10909–10924 (1988).

656   52. Z-P. Lee, K.L. Carder, and R. A. Arnone, "Deriving inherent optical properties from water color: a multiband quasi-analytical algorithm for optically deep waters," *Applied Optics,* 41, 5755-5772 (2002).

659   53. R.M. Pope, and E.S. Fry, "Absorption spectrum (380-700 nm) of pure water. II. Integrating cavity measurements," *Applied Optics,* 36, 8710-8723 (1997).

661   54. L. Kou, D. Labrie, and P. Chylek, "Refractive indices of water and ice in the 0.65-2.5 μm spectral range," *Applied Optics,* 32, 3531-3540 (1993).

663 55. P.J. Werdell, and S.W. Bailey, "An improved bio-optical data set for ocean color algorithm

664   development and satellite data product validation," *Remote Sensing of Environment,* 98,

665   122-140 (2005).

666 56. C. Dupouy, J. Neveux, and J.M. Andre, "Spectral absorption coefficient of

667   photosynthetically active pigments in the equatorial Pacific Ocean (165°E–150°W)," *Dee-*

668   *p Sea Research, Part II,* 44, 1881–1906 (1997).

669 57. J. Neveux, and F. Lantoine, "Spectrofluorometric assay of chlorophylls and pheophytins

670   using the least squares approximation technique," *Deep-Sea Research, Part I,* 40, 1747–

671   1765 (1993).

672 58. A.M. Ciotti, M.R. Lewis, and J.J. Cullen, "Assessment of the relationships between

673   dominant cell size in natural phytoplankton communities and spectral shape of the

674   absorption coefficient," *Limnology and Oceanography,* 4, 404-417 (2002).

675 59. Z-P. Lee, K.L. Carder, C.D. Mobley, R.G. Steward, and J. S. Patch, "Hyperspectral remote

676   sensing for shallow waters: 2. Deriving bottom depths and water properties by

677   optimization," *Applied Optics,* 38, 3831-3843 (1999).

678 60. S. Maritorena, A. Morel, and B. Gentili, "Diffise reflectance of oceanic shallow waters:

679   Influence of water depth and bottom albedo," *Limnol. Oceanogr.*, 39(7), 1689-1703 (1994).

680 61. S. Ouillon, Y. Lucas, and J. Gaggelli, "Hyperspectral detection of sand," *In, Proc. 7th Int.*

681   *Conf. Remote Sensing for Marine and Coastal Environments, Veridian, Miami, 20-22 May*

682   *2002* (2002).

683 62. S. J. Purkis, and R. Pasterkamp, "Integrating in situ reef-top reflectance spectra with

684   Landsat TM imagery to aid shallow-tropical benthic habitat mapping," *Coral Reefs*, 23, 5–

685   20 (2004).

686   63. B. A. Franz, "Methods for Assessing the Quality and Consistency of Ocean Color Products,

687   " http://oceancolor.gsfc.nasa.gov/REPROCESSING/R2009/validation/ (2005).

688   64. Z. P. Lee, A. Weidemann, J. Kindle, R. Arnone, K. L. Carder, and C. Davis, "Euphotic

689   zone depth: Its derivation and implication to ocean-color remote sensing," *J. Geophys. Res.*

690   112, C03009 (2007).

691   65. Z. P. Lee, "Applying narrowband remote-sensing reflectance models to wideband data",

692   *Applied Optics,* 48, 3177-3183 (2009).

693   66. R. Frouin, P-Y. Deschamps, and F. Steinmetz, "Environmental effects in ocean color

694   remote sensing," *Proc. SPIE, Ocean Remote Sensing: Methods and Applications,* Robert J.

695   Frouin, Editors, 745906 Vol. 7459, doi:10.1117/12.829871 (2009).

696   67. G. Thuillier, M. Hersé, D. Labs, T. Foujols, W. Peetermans, D. Gillotay, P.C. Simon, and

697   H. Mandel, "The Solar Spectral Irradiance from 200 to 2400 nm as Measured by the

698   SOLSPEC Spectrometer from the Atlas and Eureca Missions," *Solar Physics,* 214, 1, 1-22

699   (2003).

700   68. A. Berka, G. P. Anderson, L. S. Bernstein, P. K. Acharya, H. Dothe, M. W. Matthew, S. M.

701   Adler-Golden, J. H. Jr.Chetwynd, S. C. Richtsmeier, B. Pukall, C. L. Allred, L. S. Jeong,

702   and M. L. Hoke, "MODTRAN4 radiative transfer modeling for atmospheric correction,"

703   *Proc. SPIE Vol. 3756, p. 348-353, Optical Spectroscopic Techniques and Instrumentation*

704   *for Atmospheric and Space Research III, Allen M. Larar; Ed.* (1999).

705

706

707 **TABLE LIST**

Table 1 Symbols and Definitions

Symbol	Description	Unit
$Chla$	chlorophyll-a concentration (sum of chlorophyll-a and divinyl chlorophyll-a)	mg m^{-3}
R_{rs}	remote sensing reflectance above sea surface	sr^{-1}
r_{rs}	remote sensing reflectance just bellow sea surface	sr^{-1}
ρ_t	top of atmosphere reflectance	-
ρ_r	atmospheric molecule reflectance	-
ρ_a	aerosol reflectance, including aerosol-molecule interaction	-
ρ_g	sunglint reflectance	-
ρ_{wc}	whitecap reflectance	-
ρ_w	water-leaving reflectance	-
ρ_{ag}	aerosol + sea surface reflectance ($\equiv \rho_{a} + \rho_g + \rho_{wc}$)	-
ρ_{agw}	Rayleigh-scattering subtracted reflectance	-
t	atmospheric direct transmittance (sun-surface + surface-satellite)	-
T	direct + diffuse transmittance (sun-surface + surface-satellite)	-
τ_a	aerosol optical thickness	-
M	aerosol model number	-
λ_b	center wavelength of sensor spectral band	nm
α	power function of spectral slope of ρ_{ag}	-
c_{wl}	correction factor of spectral slope	-
pl	air-mass (=2 when satellite and sun are both in nadir)	-
a	total absorption coefficient	m^{-1}
a_w,	absorption coefficient of water	m^{-1}
a_{ph}	absorption coefficient of phytoplankton	m^{-1}
a_d	absorption coefficient of detritus	m^{-1}
a_g	absorption coefficient of CDOM	m^{-1}
a_{pg}	absorption coefficient of particles + CDOM	m^{-1}
a_{ph}'	model spectrum of phytoplankton absorption normalized at 442 nm	-
a_{dg0}	detritus+CDOM absorption at 442 nm	m^{-1}
S	spectral slope of a_{dg}'	-
a_{dg}'	model spectrum of detritus+CDOM absorption normalized at 442 nm	-
r_{pg}	ratio of a_{ph} and a_{dg} at 442 nm	-
a_{pg0}	phytoplankton+detritus+CDOM absorption at 442 nm	m^{-1}
a_{pg}'	model spectrum of phytoplankton+detritus+CDOM absorption normalized at 442 nm	-
b_b	total backscattering coefficient	m^{-1}
b_w	scattering coefficient of water	m^{-1}
b_{bw}	backscattering coefficient of water	m^{-1}
b_{bp}	backscattering coefficient of particles	m^{-1}
b_{bp0}	particle backscattering at 442 nm	m^{-1}
Y	spectral exponent of b_{bp}'	-
b_{bp}'	model spectrum of particle backscattering normalized at 442 nm	-
ρ_b	albedo of sea floor	-
H	bottom depth	m
r_{rs}^{dp}	remote-sensing reflectance for optically deep water	sr^{-1}
θ_{0w}	subsurface solar zenith angle from nadir	radian
θ_w	subsurface viewing angle from nadir	radian
θ_a	above-surface viewing angle from nadir	radian
κ	attenuation coefficient	m^{-1}
D_u^{C}	optical path-elongation factors for scattered photons from the water column	-
D_u^{B}	optical path-elongation factors for scattered photons from the bottom	-
L_{wn}	normalized water-leaving radiance	mW /μm/sr

Table 2 AVNIR-2 bands, cross-cal coefficients, and gas abruption coefficients

AVNIR-2 band number (b)	1	2	3	4
Center wavelength (λ_b) [nm]	463.0	560.0	652.1	820.6
Solar irradiance at 1 AU (F_0) [W/m^2/μm]	1943.3	1813.7	1562.3	1076.5
Calibration correction coefficients (f_{vc})	0.976	1.019	1.001	0.958
Ozone absorption coefficient (k_{oz})	1.314×10^{-5}	1.191×10^{-4}	8.697×10^{-5}	5.461×10^{-6}
Water vapor $\quad\quad k_{wv}$	0	1.763×10^{-4}	2.595×10^{-4}	1.223×10^{-3}
absorption coefficient $\quad k_{wv2}$	0	0	0	-2.580×10^{-6}
O$_2$ absorption coefficient (k_{O2})	0	0	0	1.352×10^{-4}

Table 3 Spectra of a_w, b_{bw}, and a_{ph}

	Band 1 (463.0)	Band 2 (560.0)	Band 3 (652.1)	Band 4 (820.6)	Band A (442)	Band B (555)
Central wavelength (nm)						
a_w [53]	0.01085	0.07935	0.37969	3.41656	0.00684	0.05969
b_{bw} [54]	0.00208	0.00091	0.00048	0.00018	0.00246	0.00093
(i) *New Caledonia a_{ph}*	0.84224	0.19490	0.11668	0.0	1.0	0.19869
(ii) *Picoplankton a_{ph}* [58]	0.80046	0.07025	0.11225	0.0	1.0	0.04378
(iii) *Microplankton a_{ph}* [58]	0.89368	0.37280	0.37919	0.0	1.0	0.37556

712 The values for bands 1-4 are weighted by the spectral response of the AVNIR-2 bands. The

713 a_{ph} spectra (i) is used in (A) and (D)-(F) of Table 4, (ii) and (iii) are used in (B) and (C) of

714 Table 4 respectively. Bands A and B (at 442 nm and 555 nm, respectively) were obtained

715 by weighting using a rectangular response with ±5 nm width.

**Table 4 Comparison between in situ and AVNIR-2 IOP estimates using different sets of IOP spectra**

Test No.		a_{ph} spectrum	S	Y	AVNIR-2 a_{pg} vs. in situ a_p at 442 nm×1.52			AVNIR2 vs. in situ b_{bp} at 555 nm		
					r	bias	RMSD	r	bias	RMSD
without bottom	(A) *New Caledonia*		-0.010	-1.4	0.91	0.188	0.489	0.94	0.023	0.042
	(B) ***Picoplankton*** [58]		-0.010	-1.4	0.94	0.062	0.124[−]	0.91	0.010	0.012[−]
	(C) ***Microplankton*** [58]		-0.010	-1.4	0.93	0.466	1.134[+]	0.91	0.056	0.119[+]
	(D) *New Caledonia*		**-0.018**	-1.4	0.94	0.090	0.191[−]	0.93	0.012	0.015[−]
	(E) *New Caledonia*		-0.010	**-0.0**	0.94	0.033	0.098[−]	0.93	0.012	0.015[−]
	(F) *New Caledonia*		-0.010	**-2.0**	0.91	0.340	0.909[+]	0.93	0.034	0.076[+]
with bottom	(A) *New Caledonia*		-0.010	-1.4	0.95	0.118	0.290	0.96	0.015	0.025
	(B) ***Picoplankton*** [58]		-0.010	-1.4	0.80	-0.011	0.087[−]	0.55	0.002	0.010[−]
	(C) ***Microplankton*** [58]		-0.010	-1.4	0.93	0.458[+]	1.132[+]	0.91	0.055	0.118[+]
	(D) *New Caledonia*		**-0.018**	-1.4	0.91	0.016	0.059[−]	0.75	0.005	0.009[−]
	(E) *New Caledonia*		-0.010	**-0.0**	0.72	-0.020	0.098[−]	0.49	0.004	0.012[−]
	(F) *New Caledonia*		-0.010	**-2.0**	0.91	0.315	0.898[+]	0.93	0.031	0.074[+]

720 Sample number N=15. In situ averages of $a_p \times 1.52$ at 442 nm and b_{bp} at 555 nm were 0.099

721 m^{-1} and 0.0055 m^{-1}, respectively. Superscripts $^{−}$ and $^{+}$ show values that were smaller and

722 larger compared to case (A) at significance level of 95%. S and Y are defined in the text (Eqs.
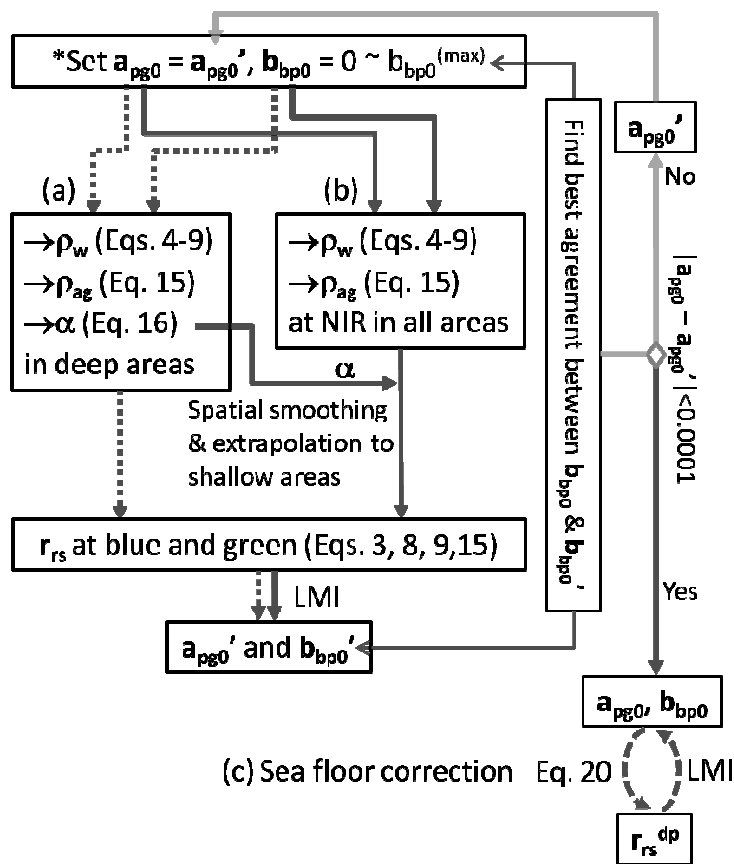
723 (12) and (13)).

724

725

726

727
728
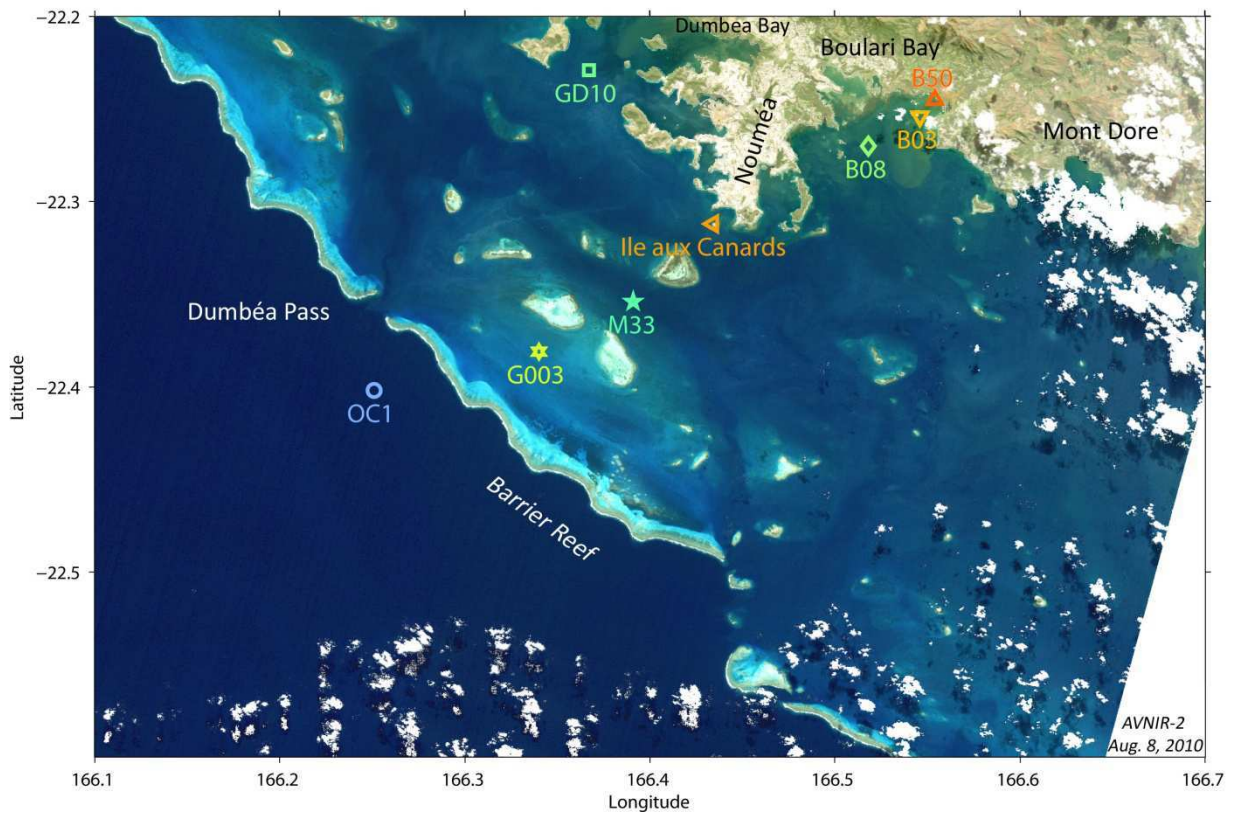
Figure 1 New Caledonia lagoon and in situ observation stations used in this study (B50, B03, B08, GD10, Ile aux Canards, M33, G003, and OC1). The background image is the RGB image of R_{rs} at 652 nm, 560 nm, and 463 nm derived from this study.
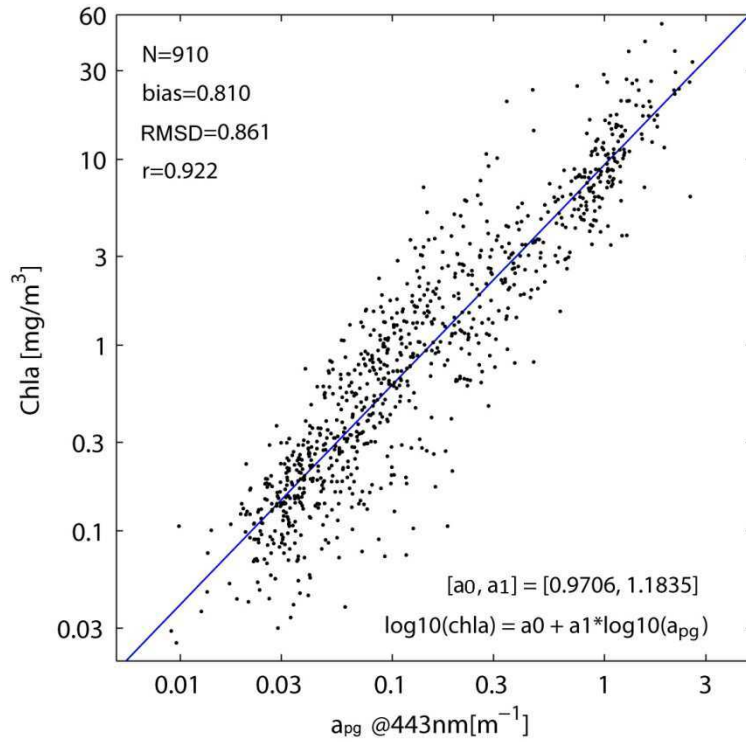
732

733

735 Figure 2 Processing flow of the IOP and aerosol correction. The operation starts from *. The

736 first flow (a) produces the α, which is used in the second flow (b). After a_{pg0} is converted ($|a_{pg0}$

737 $- a_{pg0}'| < 0.0001$), the sea-floor correction (c) is applied..

738

739

740

741 Figure 3 Relation between *Chla* and a_{pg} or blue-green R_{rs} ratio ($\log_{10}$ base) based on NOMAD

742 [55]. N, RMSD, and r indicate sample number, root mean square error of the regression ($\log_{10}$

743 scale), and the correlation. a0 and a1 are coefficients of the linear regression, *i.e.*, $\log_{10}(Chla) =$

744 $0.9706 + 1.1835 \log_{10}(a_{pg})$.

745

746
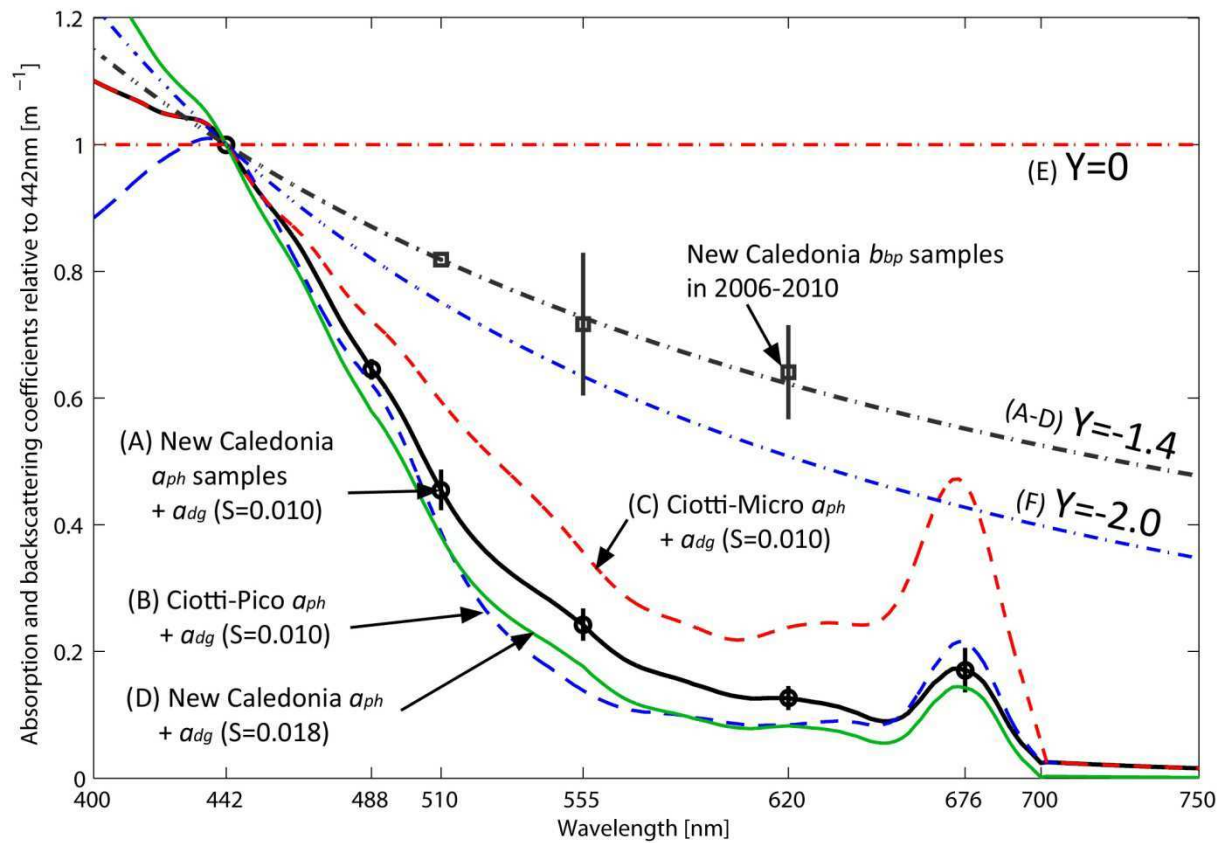
Figure 4 Model spectra of a_{pg} and b_{bp} used in this study. Models of a_{pg} (A) and b_{bp} (Y=−1.4) were set from the New Caledonia measurements. S was defined as $a_{dg}=\exp(S\times(\lambda-442))$ as in Eq. (12), and Y was defined as $b_{bp}=(\lambda/442)^{Y}$ in Eq. (13). The spectra for picoplankton (B) and microplankton (C) from [58] were used for comparison. Curves are indicated for different Y slopes for b_{bp} (Y=0 and Y=−2, see also Table 4). Bars show standard deviation of the in situ measurements.

756

757
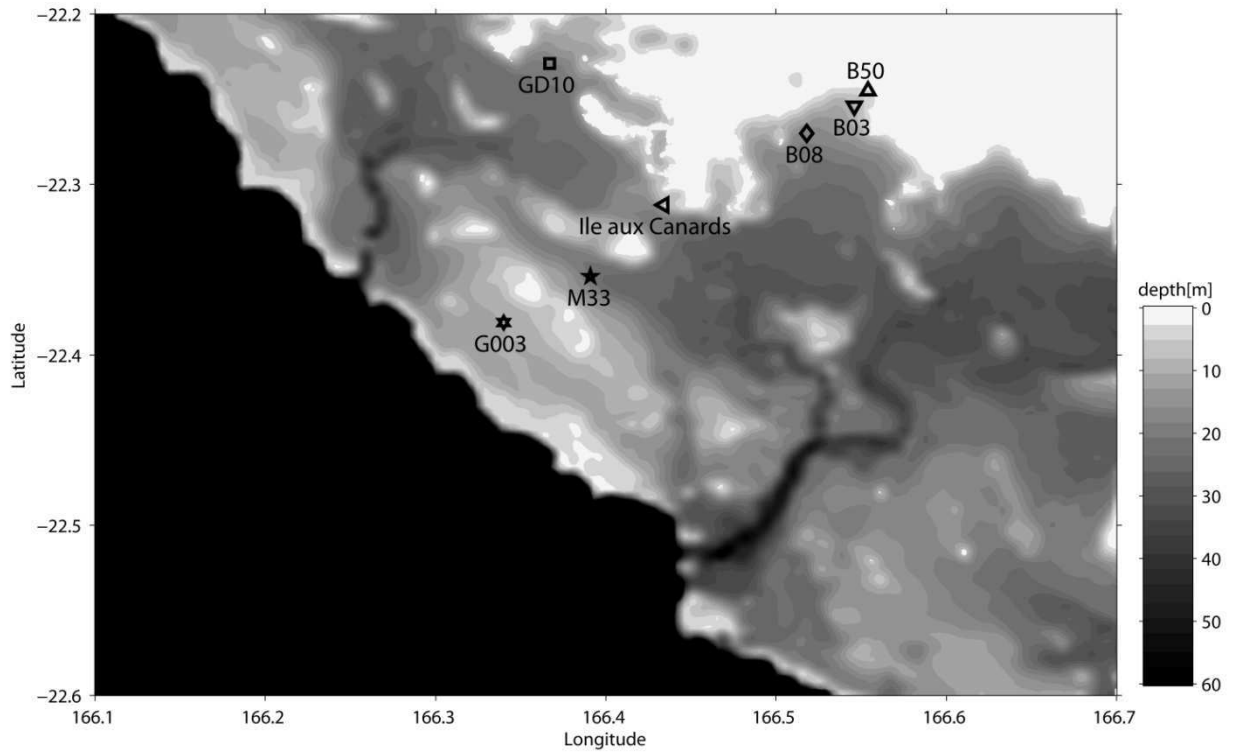
Figure 5 Bathymetry in the target area [12]. Deep areas (>60m) are filled by black.

759

Nov. 17 2008

Sep. 3 2009

(a) ρ_{agw}

(f) ρ_{agw}

(b) ρ_{ag}

(g) ρ_{ag}

(c) α

(h) α

(d) ρ_w

(i) ρ_w

(e) ρ_w (with bottom)

(j) ρ_w (with bottom)

760
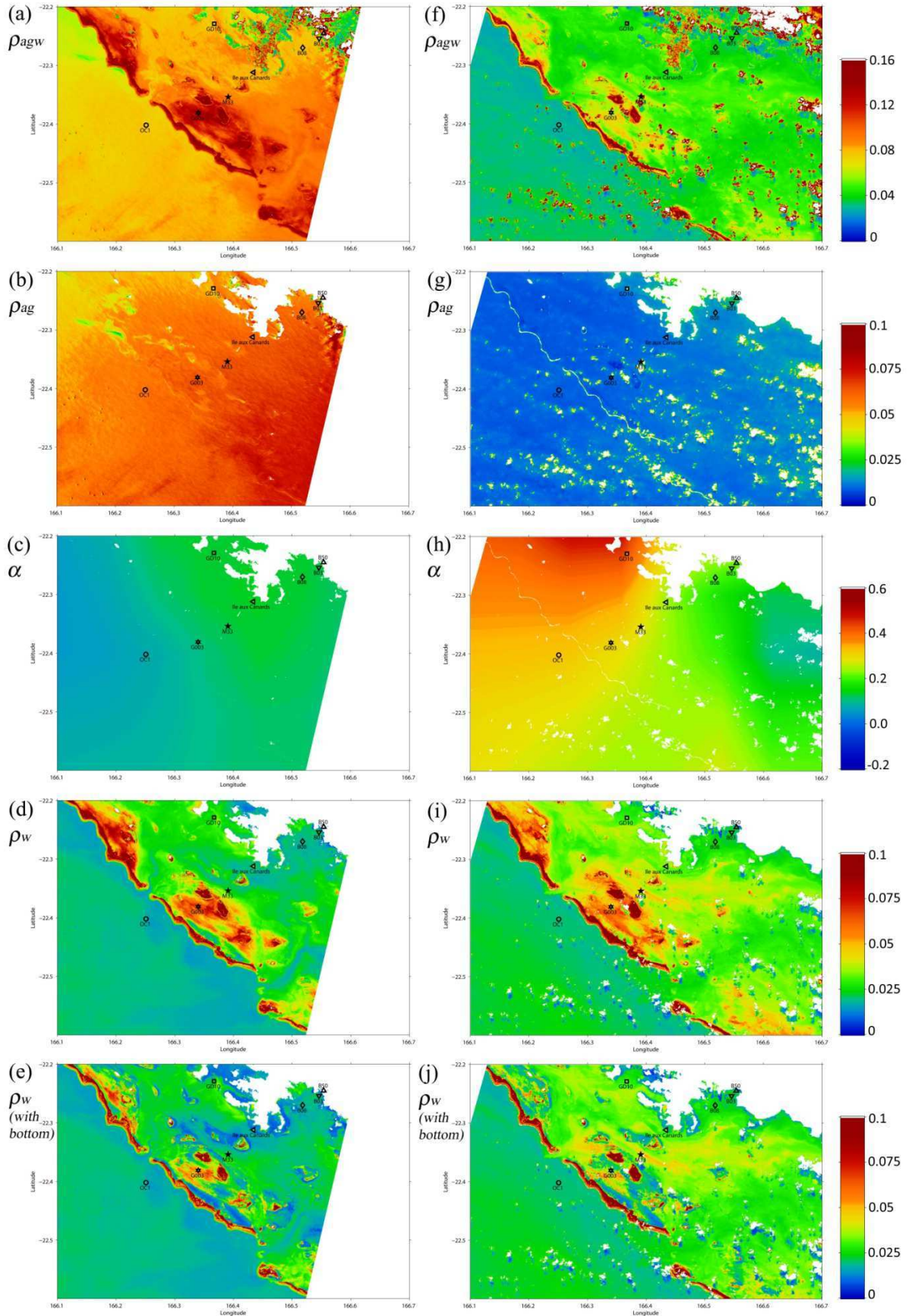
761   Figure 6 Examples of AVNIR-2-derived ρ_{agw}, ρ_{ag}, α, ρ_w without bottom correction, and ρ_w at

762   463 nm with bottom correction for 17 Nov 2008 (a-e) and for 3 Sep. 2009 (f-j) (using model

763   (A) in Table 4). The field measurement sites are shown in each panel.

764

765
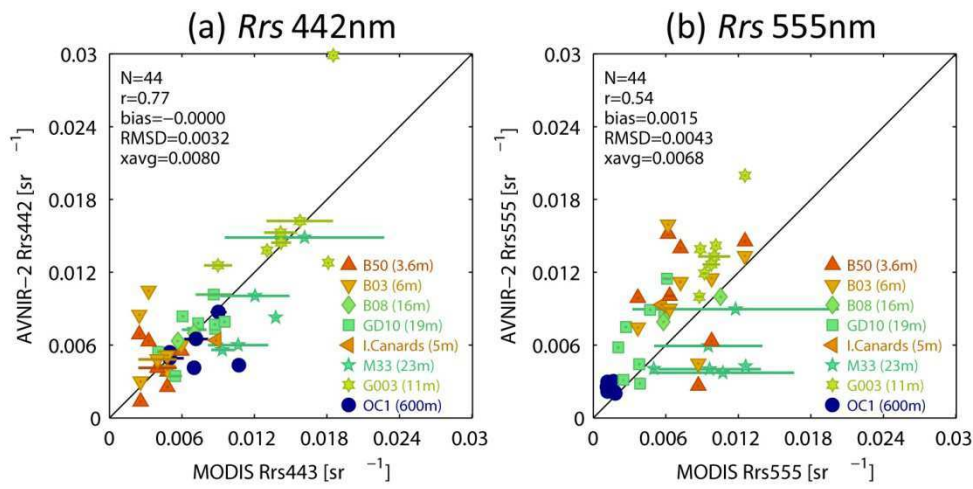
766

767

768   Figure 7 Comparison between AVNIR-2 *Rrs* at 442 nm and MODIS *Rrs* at 443 nm (a) and at

769   555 nm (b) for 44 samples. The markers distinguish between the different observation stations.

770   The horizontal bars show the standard deviation of the multiple MODIS scenes.
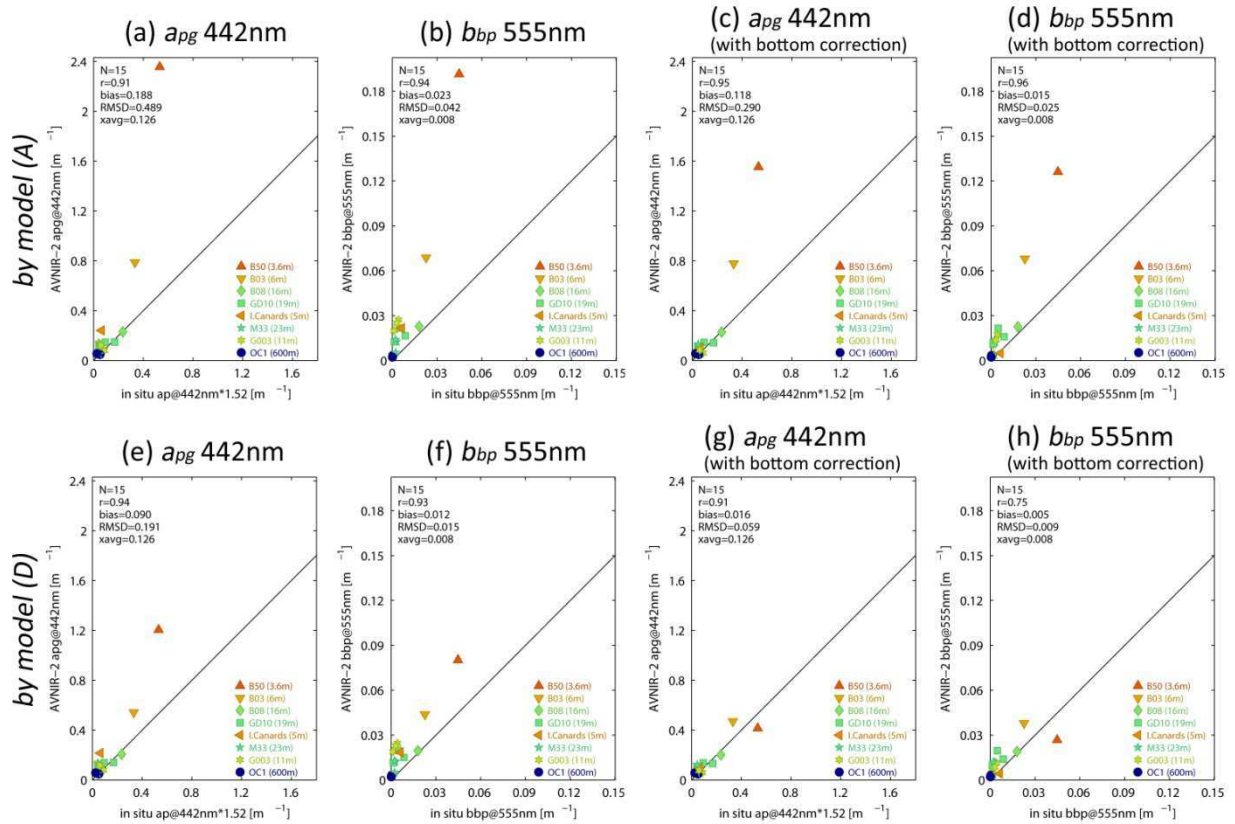
771

772

773

774
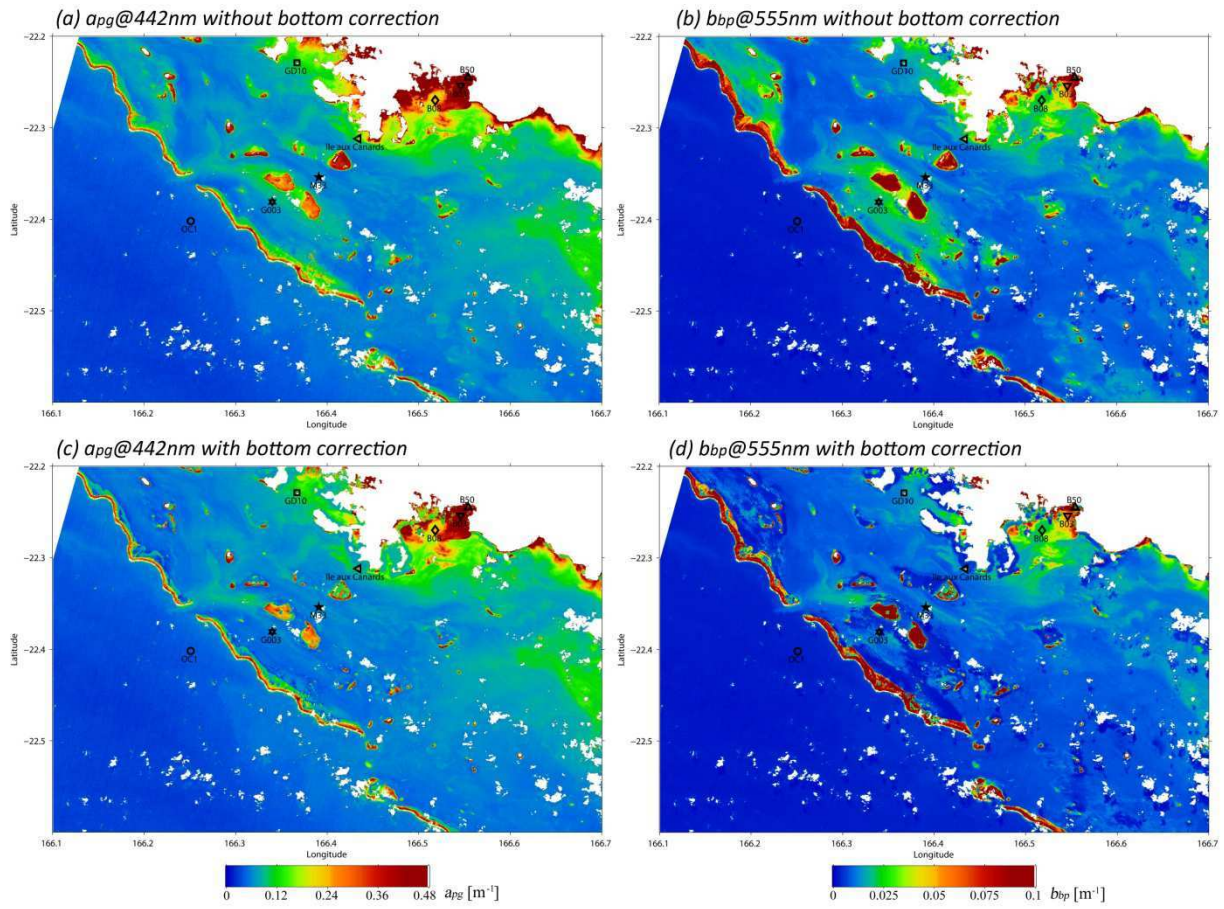
Figure 8 AVNIR-2 estimation of (a) a_{pg} at 442nm and (b) b_{bp} at 555nm on 3 Sep 2009 (using

model spectra (A) in Table 4 and no correction of the bottom reflection). (c) and (d) are same

as (a) and (b) except applying the correction of the bottom reflection. Markers show in situ

observation stations.

779

45

780


781

782

783 Figure 9 Scatter diagrams of (a) AVNIR-2 a_{pg} and in situ a_p (×1.52) at 442 nm, (b) b_{bp} at 555

784 nm from model (A) in Table 4. (c) and (d) are same as (a) and (b) except applying the

785 correction of the bottom reflection. N, r, bias, and RMSD, indicate sample number, correlation

786 coefficient, bias of AVNIR-2 from in situ, and root mean square difference. xavg indicates the

787 average of in situ data (in m^{-1}). (e)-(h) are same as (a)-(d) except they are derived from model

788 (D).

789

790

791

792
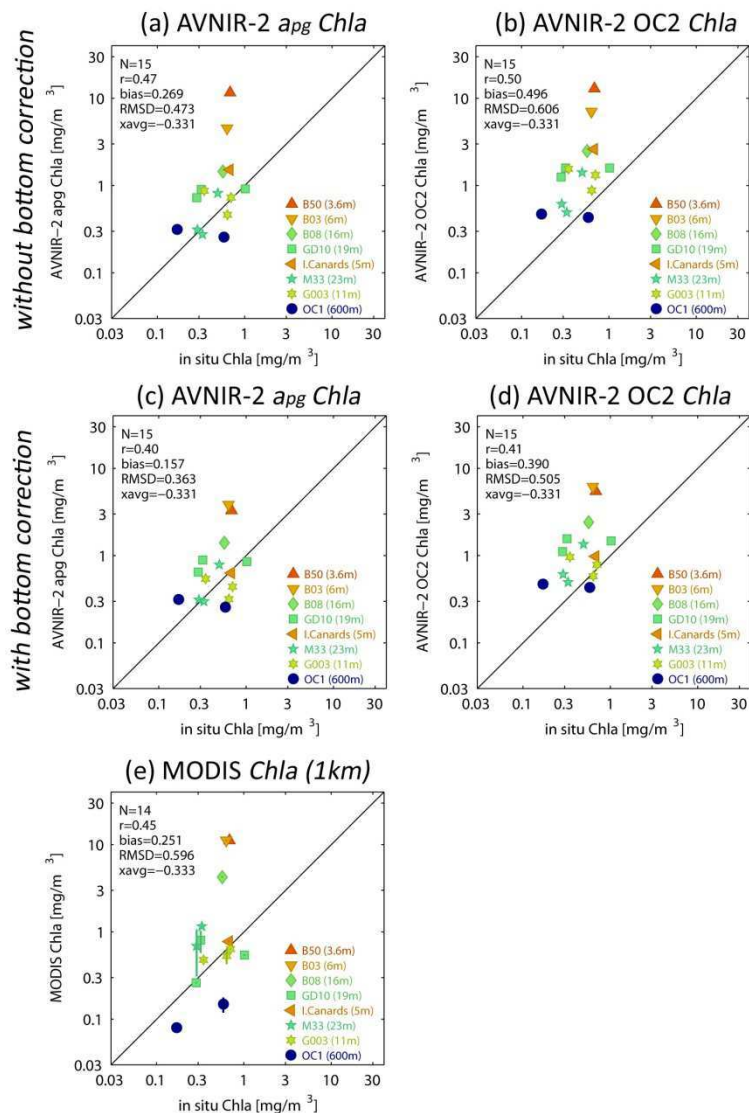
Figure 10 Scatter diagrams of in situ *Chla* and (a) *Chla* from AVNIR-2 a_{pg}, (b) *Chla* from

AVNIR-2 OC2M-HI, (c) and (d) are same as (a) and (b) except applying the bottom correction,

(e) *Chla* from the MODIS standard OC3M (1 km), and (f) the scatter plot between AVNIR-2

a_{pg} *Chla* and the MODIS OC3M *Chla*. Bars show the standard deviation of the multiple

MODIS scenes around the AVNIR-2 observation dates or the standard deviation of 3×3 pixels

of AVNIR-2 data. N, r, bias, RMSD, and xvag show sample number, correlation coefficient,

bias, root mean square difference, and the average of x-axis variables in $\log_{10}$ scale.

800

801
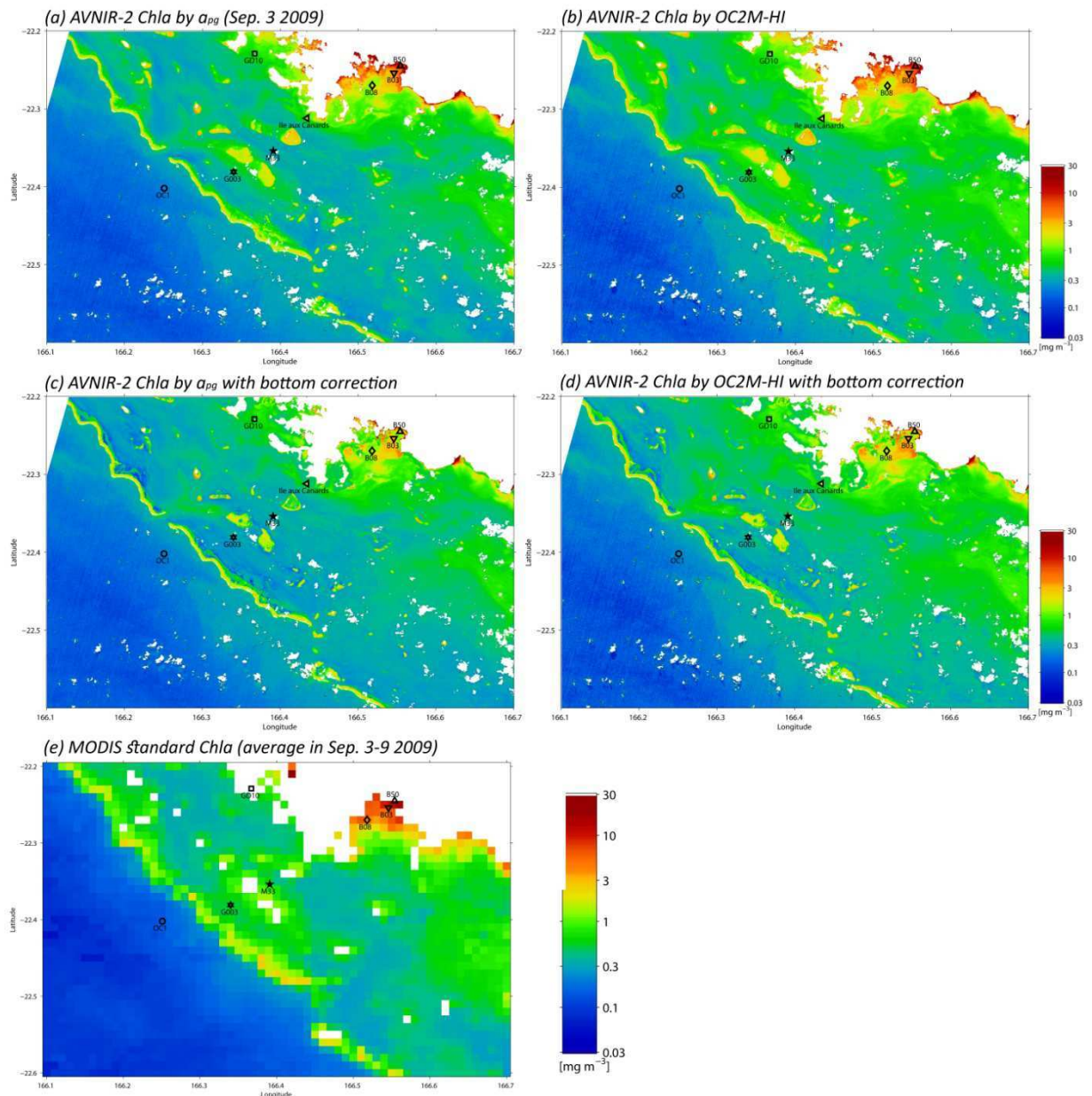
Figure 11 (a), (b), and (e) are *Chla* from a_{pg}, *Chla* from OC2M-HI (Sep. 3 2009) and the MODIS standard *Chla* (average from Sep. 3 to Sep. 9 in 2009). (c) and (d) are the same as (a) and (b) except applying the bottom correction. Markers show the in situ observation stations on Sep 9 2009.